Online model estimation and haptic characterization for robotic-assisted minimally invasive surgery

A thesis submitted in fulfilment of the requirements for the degree of Ph.D

Jaehyun Shin

M.CompEng, Korea University of Technology and Education

B.Eng (Mechatronics), Korea University of Technology and Education

School of Aerospace Mechanical and Manufacturing Engineering

College of Science Engineering and Health

RMIT University

May 2017

Declaration

I certify that except where due acknowledgement has been made, the work is that of the author alone; the work has not been submitted previously, in whole or in part, to qualify for any other academic award; the content of the thesis is the result of work which has been carried out since the official commencement date of the approved research program; any editorial work, paid or unpaid, carried out by a third party is acknowledged; and, ethics procedures and guidelines have been followed.

Jaehyun Shin

23.05.2017

List of Contents

LIST OF FIGURES

LIST OF TABLES

LIST OF ABBREVIATIONS

Abbreviations	Definition
RAS	Robotic-Assisted Surgery
RAMIS	Robotic-Assisted Minimally Invasive Surgery
FDA	The Food and Drug Administration
HC model	Hunt-Crossley model
RLS	Recursive Least Square method
UKF	Unscented Kalman Filter
AUKF	Adaptive Unscented Kalman Filter
RAUKF	Recursive Adaptive Unscented Kalman Filter
RWSTUKF	Random Weighting Strong Tracking Unscented Kalman filter

LIST OF PAPER PUBLISHED FROM THIS THESIS

[Published] J. SHIN, Y. ZHONG, J. SMITH, and C. GU, "A new parameter estimation method for online soft tissue characterization," Journal of Mechanics in Medicine and Biology, p. 1640019, (Published on 21 January 2016)

[Accepted] J. SHIN, Y. ZHONG, J. SMITH, and C. GU, “Adaptive unscented Kalman filter for online soft tissues characterization”, Journal of Mechanics in Medicine and Biology (Accepted on 19 June 2017)

[Minor revisions] J. SHIN, Y. ZHONG, J. SMITH, and C. GU, "Master-slave robotic system for needle indentation and insertion," The 6th International Conference on Biomedical Engineering and Biotechnology (ICBEB 2017) (Accepted on 13 July 2017)

[Under review] J. SHIN, Y. ZHONG, J. SMITH, and C. GU, "Adaptive online soft tissues characterization method with unknown noise statistics”, Kalman filter for online soft tissues characterization," Medical & Biological Engineering & Computing. (Submitted on 10 February 2017)

[Under review] J. SHIN, Y. ZHONG, J. SMITH, and C. GU, " Random weighting strong tracking unscented Kalman filter for soft tissue characterization", The International Journal of Medical Robotics and Computer Assisted Surgery (Submitted on 10 July 2017)

Abstract

Online soft tissue characterization is important for robotic-assisted minimally invasive surgery (RAMIS) to achieve a precise and stable robotic control with haptic feedback. The traditional linear regression method (i.e. the recursive least square (RLS) method) is inappropriate to handle nonlinear Hunt-Crossley (H-C) model since its linearization process involves unacceptable errors. This thesis presents a new nonlinear estimation method for online soft tissue characterization. To deal with nonlinear and dynamic conditions involved in soft tissue characterization, the approach expands the nonlinearity and dynamics of the H-C model by treating parameter *p* as an independent variable. Based on this, an unscented Kalman filter (UKF) was adapted for online nonlinear soft tissue characterization. A comparison analysis of the UKF and RLS methods was conducted to validate the performance of the UKF-based method.

The UKF-based method suffers from two major problems. The first one is that it requires prior noise statistics of the corresponding system to be precisely known. However, due to uncertainties in the dynamic environment of RAMIS, it is difficult to accurately describe noise characteristics. This leads to biased or even divergent UKF solutions. Therefore, in order to attain accurate estimation results from the UKF-based approach, it is necessary to estimate noise statistics online to restrain the disturbance of noise uncertainty. Secondly, the UKF performance depends on the pre-defined system and measurement models. If the models involve stochastic errors, the UKF-based solution will be unstable. In fact, the measurement model's accuracy can be guaranteed by using high-precision measurement

equipment together with a high volume of available measurement data. On the other hand, the system model is more often involved with the inaccuracy problem. In RAMIS, the system model is a theoretical approximation of the physical contact between robotic tool and biological soft tissue. The approximation is intended to fulfil the requirement of real-time performance in RAMIS. Therefore, it is essential to improve the UKF performance in the presence of system model (the contact model) uncertainty.

To address the UKF problem for inaccurate noise statistics, this thesis further presents a new recursive adaptive UKF (RAUKF) method for online nonlinear soft tissue characterization. It was developed, based on the H-C model, to estimate system noise statistics in real-time with windowing approximation. The method was developed under the condition that system noises are of small variation. In order to account for the inherent relationship between the current and previous states of soft tissue deformation involved in RAMIS, a recursive formulation was further constructed by introducing a fading scaling factor. This factor was further modified to accommodate noise statistics of a large variation, which may be caused by rupture events or geometric discontinuities in RAMIS. Simulations and comparison analyses verified the performance of the proposed RAUKF.

The second UKF limitation regarding the requirement of the accurate system model was also addressed. A random weighting strong tracking unscented Kalman filter (RWSTUKF) was developed based on the Hunt-Crossley model for online nonlinear soft tissue characterization. This RWSTUKF overcomes the problem of performance degradation in the UKF due to system model errors. It adopts a scaling factor in the predicted state covariance to compensate the inaccuracy of the system model. This scaling factor was derived by

combining the orthogonality principle with the random weighting concept to prevent the cumbersome computation from Jacobian matrix and offer the reliable estimation for innovation covariances. Simulation and comparison analyses demonstrated that the proposed RWSTUKF can characterise soft tissue parameters in the presence of system model error for RAMIS in on online mode.

Using the proposed methods, a master-slave robotic system has been developed with a nonlinear state observer for soft tissue characterization. Robotic indentation and needle insertion tests conducted to evaluate performances of the proposed methods. Further, a rupture detection approach was established based on the RWSTUKF. It was also integrated into the master-slave robotic system to detect rupture events occurred during needle insertion. The experiment results demonstrated that the RWSTUKF outperforms RLS, UKF and RAUKF for soft tissue characterization.

1. Introduction

Computer-aided systems have been broadly used in many fields because of their accurate manipulation, high-speed performance, and safety. In the medical field, Robotic-Assisted Surgery (RAS) has been developed with advanced computer technologies. Many studies and experiments have been conducted to develop therapeutic robots such as da Vinci® which is the first approved surgery robot by FDA (The Food and Drug Administration) [1]. One of the popular applications of RAS is Robotic-Assisted Minimally Invasive Surgery (RAMIS). This causes fewer traumas, less blood loss and promotes a shorter recovery time after surgery than conventional open surgeries [2-5]. However, the RAMIS only provides limited sensory information to surgeon [8]. Hence, the surgeon is required to endure a steep learning curve to conduct RAMIS.

One of the major issues of a RAMIS is the absence of contact information for a surgeon during surgery [6, 7]. In RAMIS, a surgeon performs a surgical operation based on limited visual information without touching information. Since there is no direct physical contact between the surgeon and the surgery area, the surgeon could not receive any touch cues (i.e. reaction force, temperature, vibration, skin stretch) which can be sensed by hands during conventional surgery. This restriction might prompt a cognitive overload, which could degrade the performance of a human operator (a surgeon) [8]. Haptic feedback systems for RAMIS have been researched as vital solutions to this problem [9-11].

Figure 1-1 The da Vinci® surgical system [1]

Haptic feedback systems for RAMIS have been developed with master-slave robot system. They enable a surgeon to operate surgery robot (slave-robot) and to acquire contact interaction information with haptic feedback. A surgeon performs surgery with a master-robot by controlling the movement of a slave-robot which interacts with a patient during RAMIS. The contact information between the slave-robot and the patient is conveyed to the surgeon through the master-robot.

The haptic system for RAMIS has many benefits. Firstly, the surgeon can perform surgery or be trained without the restriction of physical location. Ideally, the master-robot and slave-robot do not need to be placed in the same place. The two robots could be set in remote areas if they can exchange information through the Internet or a wireless network. Expert surgeons can train or assist a practitioner in operating surgery from the remote area. A surgeon also can perform surgery for an injured soldier on a battlefield from a safe place.

Secondly, the haptic system for RAMIS allows the surgeon to perform a micro world operation more efficiently by position and force scaling. The accuracy of position control could be improved by scaling down the movement of the slave-robot during RAMIS. Delicate movements are required in a microsurgery such as ophthalmology, otology, digit reattachment surgery, microvascular surgery, urology, and obstetrics. The performance of microsurgery can be improved by the position and force scaling approach of the haptic system for RAMIS.

Finally, the haptic system for RAMIS also can be used to prevent an application of excessive force on a patient's body or surgical sutures. Surgeon sometime applies more force than required during RAMIS because of inexperience or mistakes. The excessive force on a patient may break polypropylene sutures and tear delicate soft tissue during surgery. The unwanted damages on a patient's body or surgical sutures can be prevented by restricting the movement of the slave-robot with the haptic feedback system for RAMIS.

Sufficient information of the contact environment is required to establish a stable haptic feedback system (a master-slave system) [12]. State estimators have been proposed to characterise contact environments for master-slave robot systems including industrial applications [13-15] and medical applications [16, 17].

The main requirements of the state estimator for RAMIS are as follows: First, it should be able to estimate nonlinear characteristics of a human body in real-time [18, 19]. Besides, it should have a capability to complete the required calculations in real-time since a human body consists of heterogeneous and viscoelastic materials whose characteristics are changed in time and location.

Secondly, the state estimator should be adaptive to uncertainties such as unknown noise statistics [20]. One of the significant challenges in developing a nonlinear state estimator is the uncertainties of noise statistics [21]. The popular estimation nonlinear algorithm (unscented Kalman filter [22]) requires defining an accurate system and measurement noise covariances for optimal parameters estimation. If the pre-defined noise covariances are not accurate enough, the nonlinear estimator could be degraded or diverged [23]. In RAMIS, the noise statics could be varied during a surgical operation due to possible uncertainties such as rupture events or unwanted collisions with bones.

Finally, the performance of unscented Kalman filter is also degraded when a pre-defined system model fails to represent a current system accurately [24, 25]. The system model is required to predict the system state during UKF procedures. The inaccurately predicted state due to the model error may cause significant discrepancies of estimation in RAMIS.

1.1. Objective

The above research subjects are investigated to fulfil the following research objectives

- Review relevant literature on online soft tissue characterization method;
- Compare a linear and a nonlinear regression method in terms of soft tissue characterization;
- Investigate and develop an adaptive filtering method to deal with unknown noise statistics;
- Investigate and develop an adaptive filtering method with an existence of model error;
- Investigate and develop a master-slave system to verify proposed methods in a medical application.

This thesis focuses on the methods for characterising the contact soft tissue in the master-slave robot system under different realistic conditions of RAMIS. Firstly, the unscented Kalman filter (UKF) was employed with Hunt-Crossley (H-C) model to characterise a contact soft tissue during RAMIS. Secondly, the adaptive UKF method with the H-C model was further developed to monitor the contact soft tissue when accurate noise statistics are unknown. The random weighting strong tracking UKF was developed to improve the estimation performance even if there are model errors. Finally, a master-slave robot system was developed with the proposed characterization method to verify proposed methods in a medical application.

1.2. Contribution

The main contributions of this thesis include

- Developing an online soft tissue characterization method with nonlinear state estimator for RAMIS;
- Developing an adaptive soft tissue characterization method with unknown noise statistics for RAMIS;
- Developing an adaptive soft tissue characterization method with model error for RAMIS;
- Developing a master-slave robot system with adaptive online soft tissue characterization methods for RAMIS.

1.3. Thesis outline

The rest of this thesis is organised as follows. Chapter 2 gives a literature survey in RAMIS. Chapter 3 proposes the novel nonlinear soft tissue characterization method with the unscented Kalman filter and the Hunt-Crossley model. The adaptive nonlinear soft tissue characterization method with unknown system and measurement noise statistics are addressed in Chapter 4 (RAUKF). Chapter 5 introduces an adaptive soft tissue characterization method with a model error for RAMIS (RWSTUKF). In Chapter 6, a master-slave robotic system with rupture detection is developed based on the proposed methods

for soft tissue characterization. The presented works are concluded in Chapter 7. Figure 1-2 illustrates the organization of the thesis.

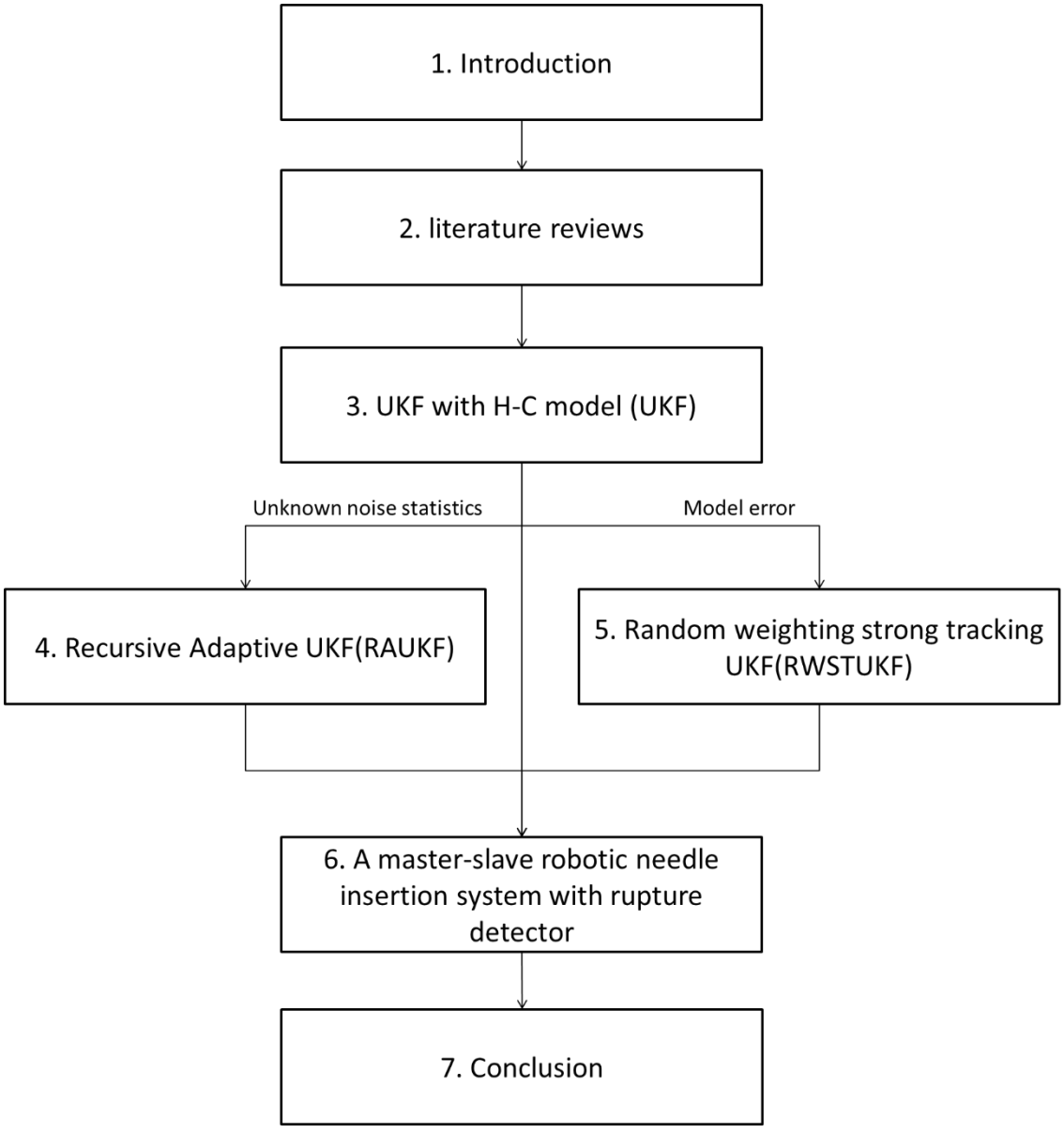

Figure 1-2 Organization of thesis

2. Literature survey

RAMIS has received considerable attentions due to its high precision, reliability and fatigueless performance. To achieve a precise and stable robot control with haptic feedback for RAMIS, the properties of soft tissue need to be taken into account. However, the soft tissue properties dynamically change with different tissue layers, regions, organs and physiological conditions. Therefore, the robotic control and haptic feedback system require the online capability of soft tissue characterization [26].

Knowledge of dynamic contact between a robotic surgical tool and soft tissue is important for online soft tissue characterization. Typically, the physics of springs and dampers are used to model the contact interaction. Various spring-damper models and associated recursive estimation algorithms have been proposed for online soft tissue characterization. Kelvin–Voigt (K-V) model or its generalised form were employed in vivo application [27]. However, this model involves unrealistic forces such as abnormal shock force and redundant sticky force at the beginning and the end of a contact, respectively [28]. The Hunt–Crossley (H-C) model eliminates the unrealistic forces involved in the K–V model. The H-C model describes the contact dynamics between an indenter and a deformable object as a nonlinear model. Diolaiti et al. reported a 2-stage method to identify soft tissue properties with the H-C model in real-time [29]. However, this approach becomes unstable when the difference between initial values and desired values is large. To address this problem, a 1-stage method was developed to improve the estimation accuracy and stability in the nonlinear environment [28]. Unfortunately, this method has a relatively slow convergence speed (i.e.

at least 90ms for a rubber ball, and 5s for a sponge and 300ms for a PVC (Polyvinyl Chloride) phantom [16]. Therefore, it is unable to satisfy the real-time requirement of RAMIS with haptic feedback. Basically, both methods require a linearization process to employ Recursive Least Square (RLS) as a parameter estimator. However, the linearization process causes a large estimation error. Moreover, employing a linear regression method is not suitable for estimating nonlinear characteristics of soft tissue [16]. Table 2-1 summarises the above existing approaches.

Table 2-1 Soft tissue characterization methods with a linear regression method

Model	Estimation method	Advantages	Drawbacks
Kelvin-Voigt	Recursive least square	Suitable for simple linear models	• Shock and redundant sticky force • Linearization error
Hunt-Crossley	2-stage method	No unrealistic forces (Shock or redundant sticky force)	• Sensitive to initial conditions • Unstable solutions • Linearization error
Hunt-Crossley	1-stage method	More robust than the 2-stage method	• Slow convergence speed • Linearization error

Comparing to the above contact models, the Finite Element Model (FEM) describes mechanical behaviours of soft tissue based on rigorous mathematical analysis of continuum mechanics [30, 31]. Although this model provides an accurate description of soft tissue, it is computationally expensive and unable to satisfy the real-time requirement of soft tissue characterization for RAMIS.

Kalman filter (KF) is a classical method for the online parameter estimation [32]. Different from the RLS, the KF can provide the minimum mean-square error estimation, even in the absence of measurement. However, this filter can only be applied to linear systems. For a nonlinear system, the Extended Kalman filter (EKF) is commonly used as an estimation approach [33]. However, the EKF suffers from problems such as large linearization errors,

cumbersome evaluation of Jacobian matrix and poor robustness against system model error [34]. Unscented Kalman filter (UKF) improves the EKF by using unscented transformation to calculate statistics of the random variable that undergoes a nonlinear transformation [35]. It estimates state mean and variance with the third-order accuracy, thus, leading to the higher estimation accuracy.

KF-based estimators, including UKF, require accurate knowledge of system and measurement noise statistics. In RAMIS, system and measurement noise statistics are usually unknown or inaccurate due to uncertainties and disturbances involved in the dynamic environment. In RAMIS, abrupt changes, such as tissue ruptures or geometric discontinuities encountered by the robotic needle, would deteriorate the estimation solution. This leads to an instability for robotic control and haptic feedback [36].

Adaptive filtering has been combined with UKF to mitigate the instability of robot control (Adaptive filtering is a method to estimate system or measurement noise statistics in real-time [37, 38]), resulting in the so-called adaptive UKF to restrain the disturbances of system and measurement noises on the filtering solution [39]. Currently, studies on the adaptive UKF are mainly dominated by researchers in the areas of signal processing, target tracking, geodetic positioning, and integrated navigation. Very limited researches have been reported on the use of the adaptive UKF for soft tissue characterization.

The adaptive filtering is established based on windowing approximation which evaluates the system or measurement noise characteristics with residuals or innovations within a small-size frame. The use of the small-size window enables the windowing approximation to offer a fast response to dynamic changes in the noise statistics. However, the limited data

available in the small-size window restricts the estimation accuracy. However, recursion [40, 41], the exact opposite to the windowing approximation, offers higher accuracy. The recursion method utilizes the entire available data via reassembling rather than limited data available in the small-size window to evaluate system characteristics at present epoch. Further, it does not retention and calculation of all data, leading to reduced computational burden. Note that algorithms, use of all available data, lead to a slow response to dynamically changing conditions.

However, the KF-based estimators require that the system model is accurately known. Predicting the current state based on the pre-defined system model with a previous state plays a key role in the KF-based estimator (i.e. EKF, UKF). When the pre-defined system model does not represent the real system precisely, estimation accuracy would be degraded or even diverged [34]. In RAMIS, the system model always involves uncertainties such as inappropriate initial conditions, modelling errors due to simplification for the purpose of computational efficiency, unexpected system noises and stochastic drifts, leading to the deteriorated UKF solutions [34, 42]. A method which can address this model error problem is required to improve the performance of the nonlinear estimator for soft tissue characterization with UKF.

To handle the disturbance of system model error on state estimation, various adaptive filters have been proposed. The fundamental idea behind these filters is that compensating the model error by adjusting the predicted state covariance in the KF algorithm. The adaptive filtering is mainly based on the concept of the windowing approximation [14]. It calculates the innovation at present time point by averaging all the historical innovations

within the window. However, due to the equal contributions of historical innovations, the windowing approximation is only suitable for the case when the innovation covariances are constant or have a small variation within the time frame. However, RAMIS involves the highly dynamic environment such as sudden changes in soft tissue deformation, rupture events in different tissue layers, and unexpected contacts with rigid bones where the innovation covariance often experiences a large variation.

Strong tracking (ST) is a relatively new concept in adaptive filtering. It incorporates a scaling factor into the predicted state covariance to compensate system model error [15-17]. In addition to the strong robustness against the system model error, the ST is also able to estimate the system states in real time. However, the ST requires cumbersome evaluations of Jacobian matrix to calculate a scaling factor. This causes an extra computational burden when the ST is used with UKF [18].

By contrast, master-slave robot systems with haptic feedback have been developed [31, 43, 44] in medical fields [45, 46]. The master-slave robot system mainly consists of five components: an operator, a master-robot, a controller (bilateral controller), a slave-robot, and a contact environment. An operator manipulates a master-robot to control a slave-robot through a bilateral controller. The slave-robot interacts with the contact environment by following behaviours of the master-robot. The contact information is delivered to the operator through the bilateral controller and the master-robot.

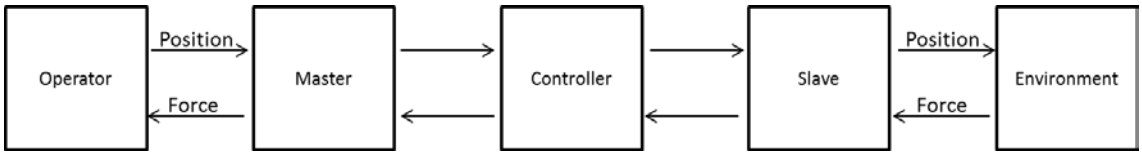

Figure 2-1 An example of a diagram of bilateral controller (Position-Force)

According to the information exchanged between the master and slave robots, bilateral controllers can be classified into Position-Position (PP), Force-Position (FP), Position-Force (PF) and Force-Force (FF). PP and PF types are the most common methods [47]. The PP bilateral controller exchanges the position information of the master and the slave robots to synchronise the behaviours of the two robots. Since it does not measure an interaction force between the slave-robot and the contact environment, the implementation is relatively easy. However, it is not suitable when the system requires an accurate manipulation [48] such as RAMIS. Conversely, the PF bilateral controller controls the slave-robot with position commands from the master-robot and delivers the force information between the slave-robot and contact environment to the operator through the master-robot. The force is either measured by a force sensor [12, 45, 46] or estimated by a disturbance observer [13, 49, 50]. Although the PF type is more complicated to be implemented, it leads to a more precise manipulation than the PP type [51]. For this reason, the PF bilateral controller has been employed for RAMIS by many researchers.

Sufficient information of system and contact environment is required to build precise PF bilateral controller [12]. The linear state observer has been employed [13, 14] to attain the adequate information of the system. However, a linear observer could not be employed to estimate the nonlinear contact environment such as soft tissue. A nonlinear state observer

is required for the nonlinear environment [20]. However, for the efficiency of the implementation, they used the linearization process, which causes estimation errors [18, 19]. To address this problem, a nonlinear state estimator for online soft tissue characterization method is required.

In summary, existing methods for real-time soft tissue characterization are mainly based on a linear contact model with a linear estimation algorithm. There has been very limited work reported on the use of the nonlinear H-C model for nonlinear soft tissue characterization. Further, the uses of the nonlinear H-C model require the development of a nonlinear estimation algorithm.

3. Unscented Kalman filter based on Hunt-Crossley model for nonlinear soft tissue characterization

3.1. Introduction

Online soft tissue characterization is of importance to RAMIS. The traditional linear regression method is inadequate for analysing the nonlinear H-C model. In addition, it requires the linearization process which leads to estimation errors. This Chapter presents a new nonlinear estimation method for dynamic characterization of mechanical properties of soft tissue. In order to deal with nonlinear and dynamic conditions in soft tissue characterization, the method extended the nonlinearity and dynamics of the H-C model by treating the parameter *p* as an independent variable. Based on this, an unscented Kalman filter was adopted for online soft tissue characterization.

3.2. Hunt-Crossley model

The H-C model describes dynamic behaviours of a nonlinear physical environment with nonlinear springs and dampers [52].

$$F = \begin{cases} Kd^n(t) + Bd^n(t)\dot{d}(t)^p & if\ d(t) \geq 0 \\ 0, & if\ d(t) < 0 \end{cases} \quad (3\text{-}1)$$

where *F, K, B,* $d(t)$ and $\dot{d}(t)$ represent the contact force, spring coefficient, damping coefficient, displacement, and velocity respectively. The power indices *n* and *p*, which are related to displacement and velocity, represent geometry variations in a contact environment. The H-C model is based on the Hertzian contact theory [52]. The *n* represents a shape of two contacted objects while the *p* expresses the relationship between the damping factor and displacement $d(t)$. Note that the larger *p* and *n* is from unity, the stronger the nonlinearity of the H-C model would be.

By considering noise q, eq.(3-1) becomes

$$F = \begin{cases} Kd^n(t) + Bd^n(t)\dot{d}(t)^p + q & if\ d(t) \geq 0 \\ 0 & if\ d(t) < 0 \end{cases} \quad (3\text{-}2)$$

Letting *p* =1, the H-C model is simplified as

$$F(t) = Kd^n(t) + Bd^n(t)\dot{d}(t) + q \quad (3\text{-}3)$$

Applying a natural logarithm to linearize eq.(3-3) for parameters estimation with a linear regression method, we have

$$ln\left(F(t)\right) = ln\,(K) + n \times ln\big(d(t)\big) + ln\left(1 + \frac{Bd\dot{(t)}}{K} + \frac{q}{Kd^n(t)}\right) \quad (3\text{-}4)$$

Since $ln(1+a) \cong a$ for $|a| \ll 1$, eq.(3-4) can be further written as

$$ln\big(F(t)\big) \cong ln(K) + \frac{B}{K}\dot{d}(t) + n \times ln\big(d(t)\big) + \frac{q}{Kd^n(t)} \quad (3\text{-}5)$$

eq.(3-5) can be simplified as

$$ln\big(F(t)\big) = \emptyset^T\boldsymbol{\theta} + \varepsilon \quad (3\text{-}6)$$

where $\emptyset^T = \left[1\,, \dot{d}(t), ln\big(d(t)\big)\right]$ is the regressor vector, $\boldsymbol{\theta} = [ln(K)\,, \frac{B}{K}\,, n]$ is the vector of dynamic parameters to be estimated, and $\varepsilon = \frac{q}{Kd^n(t)}$ is the noise.

It is evidenced that eq.(3-6) is a linear form of the H-C model. It can be used with a linear estimation method such as the RLS [28] or the classical KF [53] for parameter estimation. However, the linearization of the H-C model is under the condition that the parameter *p* is constant (i.e. *p*=1). Since biological soft tissues are heterogeneous and multi-layered and soft tissue characterization concerns the dynamic contact environment involving soft tissue deformation, parameter *p* in the H-C model must be considered as a variable. By considering the *p* as an independent variable, eq.(3-5) becomes

$$ln\big(F(t)\big) \cong ln(K) + \frac{B}{K}\dot{d}(t)^{p} + n \times ln\big(d(t)\big) + \frac{q}{Kd^{n}(t)} \tag{3-7}$$

It can easily be seen that eq.(3-7) is not linear, as $\dot{d}(t)$ in the regressor vector $\emptyset^{T}$ becomes $\dot{d}(t)^{p}$. Therefore, it is not appropriate to use a linear estimation method such as the RLS or the classic KF. Further, the linearization of the nonlinear H-C model causes estimation errors, which may lead to a biased estimation. A nonlinear estimation algorithm is required to deal with the nonlinear H-C model with the variable *p* for online soft tissue characterization.

3.3. H-C model with unscented Kalman filter

A new online soft tissue characterization method is proposed with a combination of the H-C model and UKF for RAMIS. The proposing method considers the nonlinear H-C model with the parameter *p* as a variable. It adopts the UKF to deal with the nonlinearity of the H-C model.

The use of UKF for parameter estimation requires a system state vector, a system and a measurement model. To meet the requirements, we firstly define a system state as

$$\boldsymbol{x}_k = [d(t)_k\,,\, \dot{d}(t)_k\,,\; F_k\,,\, K_k\,,\, B_k\,,\, n_k\,,\, p_k\,] \tag{3-8}$$

where $\boldsymbol{x}_k$ the system sate vector and k is the time point. The system state model is described as

$$\boldsymbol{x}_k = f(\boldsymbol{x}_{k-1}) + \boldsymbol{q}_{k-1} = \begin{Bmatrix} d_{k-1} + \dot{d}_{k-1} \times \Delta t_{k-1} \\ \dot{d}_{k-1} \\ K_{k-1} d_{k-1}^{n_{k-1}} + B_{k-1} d_{k-1}^{n_{k-1}} \dot{d}_{k-1}^{p_{k-1}} \\ K_{k-1} \\ B_{k-1} \\ n_{k-1} \\ p_{k-1} \end{Bmatrix} + \boldsymbol{q}_{k-1} \tag{3-9}$$

where $\boldsymbol{q}_k \sim (0, \boldsymbol{Q}_k)$ is the system noise, which is assumed as white Gaussian noise with zero mean and covariance $\boldsymbol{Q}_k$, $f(\cdot)$ is the system function, which represents the relationship between the system states at time points t_k and t_{k-1}, and Δt_{k-1} is the time step.

The measurement function is defined as

$$\boldsymbol{y}_k = h(\boldsymbol{x}_k) + \boldsymbol{r}_k = \begin{pmatrix} d_k \\ F_k \end{pmatrix} + \boldsymbol{r}_k \tag{3-10}$$

where $\boldsymbol{y}_k$ denotes the measurement vector, $h(\cdot)$ is the measurement function, which describes the relationship between the system state and the measurement, and $\boldsymbol{r}_k \sim (0, \boldsymbol{R}_k)$ is the measurement noise, which is also assumed as white Gaussian noise with zero mean and covariance $\boldsymbol{R}_k$. Based on these definitions, the detailed algorithm of UKF is then followed.

3.4. Unscented Kalman filter

Step 1 Initialization

$$\widehat{\boldsymbol{x}}_0 = E(\boldsymbol{x}_0) \tag{3-11}$$

$$\widehat{\boldsymbol{P}}_0 = E[(\boldsymbol{x}_0 - \widehat{\boldsymbol{x}}_0)(\boldsymbol{x}_0 - \widehat{\boldsymbol{x}}_0)^T] \tag{3-12}$$

where $\boldsymbol{x}_0$ is the pre-defined initial state.

Step 2 Time updating

1) Select sigma points as follows

$$\widehat{\boldsymbol{x}}_{k-1}^{(i)} = \widehat{\boldsymbol{x}}_{k-1} + \widehat{\boldsymbol{x}}^{(i)} \ (i = 1, \cdots, 2N) \tag{3-13}$$

$$\widehat{\boldsymbol{x}}^{(i)} = \left(\sqrt{(N+\lambda)\widehat{\boldsymbol{P}}_{k-1}} \right)_i^T \ (i = 1, \cdots, N)$$

$$\widehat{\boldsymbol{x}}^{(N+i)} = -\left(\sqrt{(N+\lambda)\widehat{\boldsymbol{P}}_{k-1}} \right)_i^T \ (i = 1, \cdots, N)$$

where N is the dimension of state vector $\boldsymbol{x}$, the parameter λ is defined as $\lambda = \alpha^2(N+k) - N$ with constant α, and $\widehat{\boldsymbol{P}}_{k-1}$ is the estimated state covariance at time point t_{k-1} (k = 1,2,…).

2) Calculation of predicted state vector $\overline{\boldsymbol{x}}_k$ based on the selected sigma points

$$\overline{\boldsymbol{x}}_k^{(i)} = f(\widehat{\boldsymbol{x}}_{k-1}^{(i)}) \tag{3-14}$$

$$\overline{\boldsymbol{x}}_k = \frac{1}{2N} \sum_{i=1}^{2N} w_i^m \, (\overline{\boldsymbol{x}}_k^{(i)})$$

3) Calculation of predicted state covariance $\overline{\boldsymbol{P}}_k$

$$\overline{\boldsymbol{P}}_k = \sum_{i=1}^{2N} w_i^c \left(\overline{\boldsymbol{x}}_k^{(i)} - \overline{\boldsymbol{x}}_k\right)\left(\overline{\boldsymbol{x}}_k^{(i)} - \overline{\boldsymbol{x}}_k\right)^T + \boldsymbol{Q}_k \tag{3-15}$$

$$\begin{cases} w_0^m = \dfrac{\lambda}{N+\lambda} \\ w_0^c = \dfrac{\lambda}{N+\lambda} + (1-\alpha^2+\beta) \\ w_i^m = w_i^c = \dfrac{1}{2(N+\lambda)} \qquad i = 1, \ldots, 2N \end{cases}$$

where w_i^m and w_i^c are the mean and covariance weights, N is the dimension of state vector $\boldsymbol{x}$, and α and β are constants.

Step 3 Measurement updating

1) Calculation of predicted measurement $\overline{\boldsymbol{y}}_k$

$$\overline{\boldsymbol{y}}_k^{(i)} = h(\overline{\boldsymbol{x}}_k^{(i)}) \tag{3-16}$$

$$\overline{\boldsymbol{y}}_k = \frac{1}{2N}\sum_{i=1}^{2N} w_i^m (\overline{\boldsymbol{y}}_k^{(i)})$$

2) Calculation of predicted measurement covariance $\boldsymbol{P}_{\overline{\boldsymbol{y}}_k}$

$$\boldsymbol{P}_{\overline{\boldsymbol{y}}_k} = \sum_{i=1}^{2N} w_i^c \left(\overline{\boldsymbol{y}}_k^{(i)} - \overline{\boldsymbol{y}}_k\right)\left(\overline{\boldsymbol{y}}_k^{(i)} - \overline{\boldsymbol{y}}_k\right)^T + \boldsymbol{R}_k \tag{3-17}$$

where $\overline{\boldsymbol{y}}_k^{(i)}$ is the selected sigma point of the predicted measurement, which are obtained in the same way as eq.(3-15).

3) Calculation of the cross covariance between $\overline{\boldsymbol{x}}_k$ and $\overline{\boldsymbol{y}}_k$

$$\boldsymbol{P}_{\overline{\boldsymbol{x}}_k \overline{\boldsymbol{y}}_k} = \sum_{i=1}^{2N} w_i^c \left(\overline{\boldsymbol{x}}_k^{(i)} - \overline{\boldsymbol{x}}_k\right)\left(\overline{\boldsymbol{y}}_k^{(i)} - \overline{\boldsymbol{y}}_k\right)^T \tag{3-18}$$

4) Calculation of the Kalman gain

$$\boldsymbol{K}_k = \boldsymbol{P}_{\bar{x}_k \bar{y}_k} \boldsymbol{P}_{\bar{y}_k}^{-1} \tag{3-19}$$

5) Updating the estimated state and associated covariance

$$\hat{\boldsymbol{x}}_k = \bar{\boldsymbol{x}}_k + \boldsymbol{K}_k(\boldsymbol{y}_k - \bar{\boldsymbol{y}}_k) \tag{3-20}$$

$$\hat{\boldsymbol{P}}_k = \bar{\boldsymbol{P}}_k - \boldsymbol{K}_k \boldsymbol{P}_{\bar{y}_k} \boldsymbol{K}_k^T \tag{3-21}$$

Repeat **Step 2-3** every time step.

We can estimate current state, which is $\hat{\boldsymbol{x}}_k$ in a nonlinear and noisy environment by repeating the algorithm above.

3.5. Verification and discussion

Simulations were conducted to evaluate the performance of the proposed method based on the measured displacements and interaction forces. Subsequently, the output force was reconstructed with the estimated nonlinear parameters of the H-C model and the input displacement data. Further, the output force was compared with the interaction force reference values to validate the proposed method. Comparison with a linear regression method such as RLS was also conducted. In the experiments, initial values for system state covariance $\boldsymbol{P}_0$, system state noise covariance $\boldsymbol{Q}_0$ and measurement noise covariance $\boldsymbol{R}_0$ were set as a 7 x 7 identity matrix for the proposed UKF.

The performance evaluation focuses on three different cases, where the measurement data were obtained from the literature [54, 55]. The first two cases consider the H-C model with

the constant *p* (*p*=1). One case is with an interaction force of small variation, indicating the test subject is homogeneous. The other is with an interaction force of large variations, which indicates that the test subject is a heterogeneous material which has multiple layers as the peak force values represent the ruptures existing in the test subject. The third case is under the same test conditions as the heterogeneous subject case except that the parameter *p* is considered as an independent variable. The proposed UKF method was compared with the RLS in the case of constant parameter *p*. The results for the cases with the parameter *p* as a constant and or a variable under the heterogeneous and multi-layer test subject were compared to study the effect of the parameter *p* on parameter estimation. For the two cases with parameter as a constant (*p*=1), the RLS method involves the linearization of the H-C model, while the proposed UKF uses the nonlinear H-C model where the nonlinearity consists of the item $d^n(t)$ only. For the case with parameter *p* as a variable, the nonlinearity of the H-C model consists of both items $d^n(t)$ and $\dot{d}(t)^p$. To differentiate the UKFs between the case with the parameter *p* as a constant (*p*=1) and the case with the parameter *p* as a variable, the UKF for the cases with parameter *p* as a constant (*p*=1) is named UKF1 and the UKF for the case with the parameter *p* as a variable is named UKF2. Table 4-6 compares the estimation errors from these three methods.

3.5.1. Case 1: Homogeneous soft tissue (p=1)

The input data were formulated based on the force profile from the conducted experiment [54]. The interaction force was measured when a needle was inserted into a soft tissue by a needle insertion robot at 10 mm/s speed. The interaction force represents an example of the situation when a needle is inserted into a homogenous soft tissue. Figure 3-1 shows that the variation of the interaction force is not dynamic in the black line. In this chapter, the interaction force profile is defined as stationary input data because the variation is negligible. The measured interaction force has 1 kHz sampling rate at 10 mm/s constant insertion speed. The initial values for the state parameters were $\boldsymbol{x}_0$ = [0.1, 0.1, 0.01, 0.0001, 0.0001, 1].

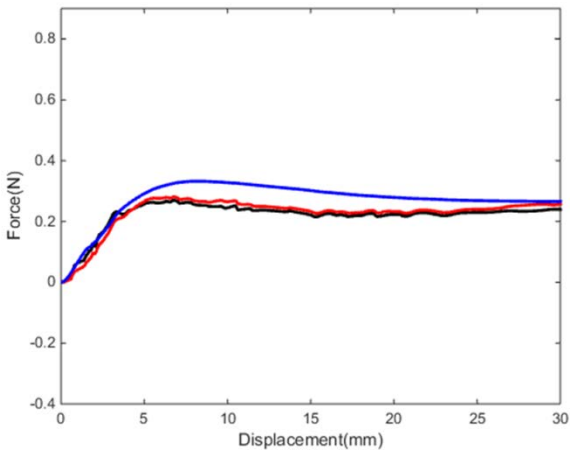

Figure 3-1 The estimation results of UKF1 and RLS for the case with p as constant (p=1) and subject to the homogeneous test sample: The black, red and blue line indicates the reference values and estimations of UKF1 and RLS, respectively

A MATLAB program was developed to estimate nonlinear parameters of the H-C model with the UKF and RLS to compare the estimation performance in nonlinear environments. The result data of RLS were simulated with a 1-stage method [28]. In order to compare results, the interaction force is reconstructed with the estimated nonlinear parameters of the H-C model and input displacement data. Figure 3-1 shows the estimations from both UKF1 and RLS for the case with the parameter p as a constant (p = 1) and subject to the homogeneous test sample. Although both estimations were converged to the reference value, the estimation by UKF1 is much closer to the reference values than that of the RLS. The mean error is 29.30mN for UKF1 and 34.02mN for RLS. This demonstrates that although both UKF1 and RLS are effective for handling homogeneous soft tissue, UKF1 with the nonlinear H-C model has higher accuracy than RLS with the linearized H-C model. Table 2-1 compares detailed error analysis of two methods.

3.5.2. Case 2: Heterogeneous soft tissue (p=1)

A simulation was conducted for the case when a needle is inserted into heterogeneous soft tissue. The simulation was designed for the case when a needle pierces through a multi-layer skin. The input data of the simulation were displacement, and the interaction force of the needle. The output data were the reconstructed force based on the estimated nonlinear parameters of H-C and the input displacement is the same as **Case 1**. The interaction force was generated based on the experiment data [55] measured when a needle is inserted into soft tissue. The interaction force is abruptly changed as the needle penetrates different

layers. The generated interaction force has a 1 kHz sampling rate at 10 mm/s constant insertion speed. The initial values for state parameters were $\boldsymbol{x}_0$ = [0.1, 0.1, 0.01, 0.0001, 0.0001, 1].

Figure 3-2 shows the results for the case with the parameter *p* as a constant (*p*=1) but under the heterogeneous and multi-layer test subject, where the fluctuations (such as the one at 37mm) in the force data (reference data) indicate the ruptures of different tissue layers [55]. It can be seen that the estimation curve of UKF1 still follows the reference curve, while the RLS curve failed to do so. The mean error is 54.1mN for UKF1, while 295.36mN for RLS. This demonstrates that RLS is incapable of handling heterogeneous and multi-layer soft tissue. However, although UKF1 can handle heterogeneous and multi-layer soft tissue, its performance is unsatisfactory. It leads to a large estimation error after the displacement of 37 mm.

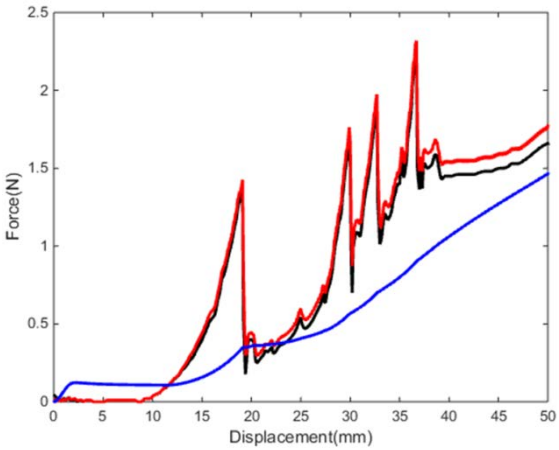

Figure 3-2 The estimation results of both RLS and UKF1 for the case with *p* as constant (*p=1*) but subjected to a heterogeneous and multi-layer test sample: The black, red and blue line indicates the reference values and estimations of UKF1 and RLS, respectively

3.5.3. Case 3: Heterogeneous soft tissue (*p* is not unity)

The simulation conditions of **Case 3** were the same as **Case 2** in Section 3.5.2 except the *p* was considered as a variable so it was estimated during simulation. The simulation result shows the effect of a non-constant *p*.

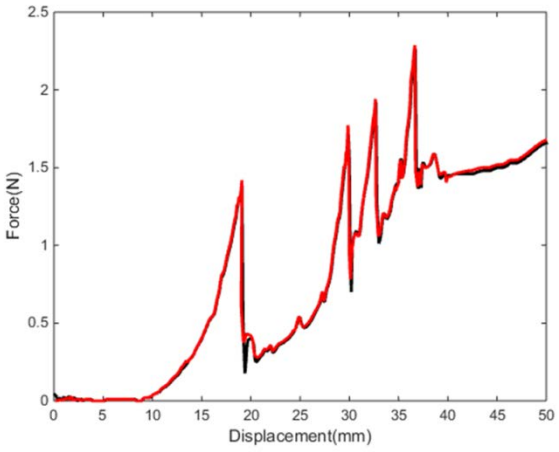

Figure 3-3 The estimation results of UKF2 for the case under the same test conditions as Figure 3-2 except for the parameter *p* as a variable: The black and red line the reference values and estimations of UKF2

Figure 3-3 shows the results for the case under the same test conditions in Figure 3-2 except that the parameter *p* is a variable. It can be seen that the estimated curve of UKF2 is very close to the reference curve during the entire displacement range. Compared to Figure 3-2, it is also evidenced that UKF1 with the parameter *p* as a constant (*p*=1) has a larger estimation error than UKF2 with the parameter *p* as a variable. In particular, after the displacement of 37mm, the estimation curve of UKF2 is almost the same as the reference curve, while the UKF1 estimation curve has a large deviation from the reference curve without showing any convergence trend. The mean estimation error is 11.00mN for UKF2,

but is 54.10mN for UKF1. This demonstrates that UKF2 has the capability to deal with heterogeneous and multi-layer soft tissue due to the use of parameter *p* as a variable, while UKF1 is incapable of doing so as it treats the parameter *p* as a constant (*p*=1). Table 3-1 provides the detailed comparison of three cases in terms of maximum, minimums and means errors.

Table 3-1 Estimation errors of RLS and UKF

Simulation Case		RLS (mN)			UKF (mN)			
		Max	**Min**	**Mean**		**Max**	**Min**	**Mean**
Constant *p* (*p*=1)	Homogeneous soft tissue	86.45	0.02	34.02	UKF1	110.50	0.08	29.30
	Heterogeneous and multi-layer soft tissue	1368.51	0.001	295.36		294.94	0.000	54.10
Variable *p*	Heterogeneous and multi-layer tissue				UKF2	198.40	0.000	11.00

By treating the *p* as an additional variable, the dimension of the system state vector is increased by one. It leads to an increased computational load of the proposed method. Simulations were conducted to compare the computational performances of UKF1 and UKF2 under the same conditions to verify the efficiency of the proposed method. Figure 3-4 shows the computing times of each iteration for both UKF1 and UKF2. It can be seen that treating the *p* as an additional variable does not significantly increase the computing time. The average computing time of iteration for UKF2 was 1.1263ms, which was only 6.9% more than that for UKF1 whose computing time was 1.0535ms.

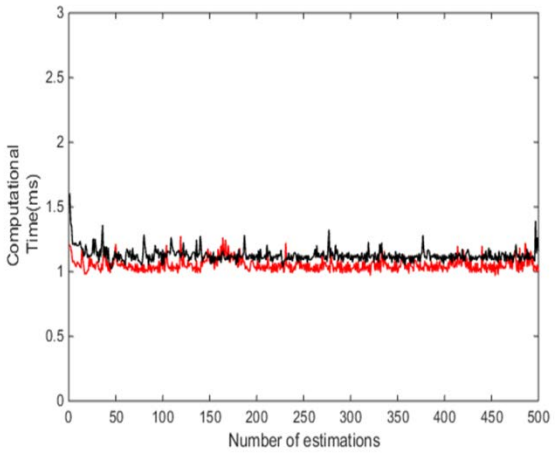

Figure 3-4 The computing time for each estimation for UKF1 and UKF2: The black and red line indicates the computing time of UKF1 and UKF2

3.6. Summary

This chapter presents a new nonlinear parameter estimation method by combining the nonlinear H-C model with the nonlinear filtering algorithm (UKF) for online soft tissue characterization. This method treats the parameter *p* of the H-C model as a variable to deal with nonlinear and dynamic conditions in soft tissue characterization. Based on the nonlinear H-C model, UKF is adopted for the online estimation of soft tissue parameters. Simulations and comparison analyses verified that the proposed method can take into account heterogeneous and multi-layer soft tissue, and its performance is therefore much better than that of RLS.

4. Adaptive recursive unscented Kalman filter for nonlinear soft tissue characterization in the presence of noise statistics uncertainty

4.1. Introduction

In Chapter 3, the online soft tissue characterization method was proposed by combining the UKF with the H-C model. The UKF-based approach assumes that noise statistics of a system is accurately known. However, it is difficult to define system and measurement noise covariances accurately and sometimes their values change over time. When the pre-defined noise statistics fail to precisely describe the system, the UKF-based method will have a large estimation error and can be diverged.

To solve this problem, this chapter presents a new nonlinear recursive adaptive filtering methodology. It does this by joining windowing approximation with recursion into UKF for online nonlinear soft tissue characterization for RAMIS. An Adaptive UKF, based on the H-C model, was developed using windowing approximation to estimate soft tissue parameters under unknown noise statistics of small variation. Based on this, a recursive adaptive UKF was developed with a weighting factor to improve estimation accuracy. Further, this weighting factor was modified to accommodate noise statistics of large variation. This large variation could be caused by rupture events or geometric discontinuities in RAMIS. Note that the RAUKF with the standard weighting factor could not account the variation in the

noise covariance if the variation is bigger than three times than the initial value (i.e. initial value $0.004N^2$ and the varied value $0.012N^2$). Simulations and experiments, as well as comparison analysis, have been conducted to comprehensively evaluate the performance of the proposed method for soft tissue characterization.

4.2. Adaptive unscented Kalman filter

The conventional UKF requires prior knowledge on system and measurement noise covariances ($\boldsymbol{Q}_k$ and $\boldsymbol{R}_k$). However, in practice, they are usually unknown or inaccurate due to environmental uncertainties and disturbances. If the measurement noise covariance involves uncertainty, the predicted measurement covariance $\boldsymbol{P}_{\bar{y}_k}$ will become inaccurate. This leads to a biased Kalman gain $\boldsymbol{K}_k$. Thus, the state estimate obtained from eq.(3-20) will be deteriorated. Similarly, if the system noise covariance involves uncertainty, it will affect the predicted state $\bar{\boldsymbol{x}}_k$ and the predicted measurement $\bar{\boldsymbol{y}}_k$, leading to the deterioration to the estimated state $\hat{\boldsymbol{x}}_k$.

In this chapter, a new recursive adaptive UKF was developed by combining windowing approximation with recursion into an online estimation of system and measurement noise covariances via covariance matching.

4.2.1. Estimation of system noise covariance

By introducing an adaptive scaling factor Φ, the system noise covariance can be represented as

$$\boldsymbol{Q}_k = \Phi \boldsymbol{Q}_{k-1} \tag{4-1}$$

Substituting eq.(4-1) into eq.(3-15), the predicted state covariance can be modified as

$$\bar{\boldsymbol{P}}_k^{\boldsymbol{m}} = \sum_{i=1}^{2N} w_i^c \left(\bar{\boldsymbol{x}}_k^{(i)} - \bar{\boldsymbol{x}}_k\right)\left(\bar{\boldsymbol{x}}_k^{(i)} - \bar{\boldsymbol{x}}_k\right)^T + \Phi \boldsymbol{Q}_{k-1} \tag{4-2}$$

It can be seen from eq.(4-2) that we can online adjust the system noise covariance via the adaptive scaling factor Φ.

Denote residual vector $\boldsymbol{Z}_k^R$ as

$$\boldsymbol{Z}_k^R = \boldsymbol{y}_k - \bar{\boldsymbol{y}}_k^+ \tag{4-3}$$

where the $\bar{\boldsymbol{y}}_k^+$ is calculated with the estimated state as

$$\bar{\boldsymbol{y}}_k^{+(i)} = h(\hat{\boldsymbol{x}}_k^{(i)}) \tag{4-4}$$

$$\bar{\boldsymbol{y}}_k^+ = \frac{1}{2N} \sum_{i=1}^{2N} w_i^m (\bar{\boldsymbol{y}}_k^{+(i)})$$

In theory, the residual covariance can be directly calculated from the residual vector $\boldsymbol{Z}_k^R$ as

$$\boldsymbol{COV}_{\boldsymbol{Z}_k^R} = E(\boldsymbol{Z}_k^R \boldsymbol{Z}_k^{R^T}) \tag{4-5}$$

Introducing a windowing approximation to calculate the expectation in eq.(4-5), we readily

$$\boldsymbol{COV}_{\boldsymbol{Z}_k^R} = \frac{1}{m}\sum_{j=1}^{m} \boldsymbol{Z}_{k-j}^R \, \boldsymbol{Z}_{k-j}^{R\,T} \tag{4-6}$$

where *m* is called the window size, which is the number of the state vectors within the time window (t_{k-m}, t_{k-1}).

By the approximation of Taylor series, eq.(3-17) could be defined as

$$\begin{aligned} \boldsymbol{P}_{\bar{\boldsymbol{y}}_k} &= \sum_{i=1}^{2N} w_i^c \left(\bar{\boldsymbol{y}}_k^{(i)} - \bar{\boldsymbol{y}}_k\right)\left(\bar{\boldsymbol{y}}_k^{(i)} - \bar{\boldsymbol{y}}_k\right)^T + \boldsymbol{R}_k \\ &= \boldsymbol{H}_k \bar{\boldsymbol{P}}_k \boldsymbol{H}_k^T + \boldsymbol{R}_k \end{aligned} \tag{4-7}$$

where $\boldsymbol{H}_k = \left.\frac{\partial h(\boldsymbol{x})}{\partial \boldsymbol{x}}\right|_{\boldsymbol{x}=\hat{\boldsymbol{x}}_{k-1}}$.

The UKF based estimator is ideal when the condition of eq.(4-8) is met [56]

$$\boldsymbol{COV}_{\boldsymbol{Z}_k^R} = \boldsymbol{R}_k - \boldsymbol{H}_k \hat{\boldsymbol{P}}_k \boldsymbol{H}_k^T \tag{4-8}$$

With eq.(3-21), eq.(4-8) becomes as

$$\boldsymbol{COV}_{\boldsymbol{Z}_k^R} = \boldsymbol{R}_k - \boldsymbol{H}_k\left(\bar{\boldsymbol{P}}_k - \boldsymbol{K}_k \boldsymbol{P}_{\bar{\boldsymbol{y}}_k} \boldsymbol{K}_k^T\right)\boldsymbol{H}_k^T \tag{4-9}$$

Substituting eq.(4-2) and eq.(4-7) into eq.(4-9)

$$\boldsymbol{COV}_{\boldsymbol{Z}_k^R} = \boldsymbol{R}_k - \boldsymbol{H}_k\left(\sum_{i=1}^{2N} w_i^c \left(\bar{\boldsymbol{x}}_k^{(i)} - \bar{\boldsymbol{x}}_k\right)\left(\bar{\boldsymbol{x}}_k^{(i)} - \bar{\boldsymbol{x}}_k\right)^T + \Phi \boldsymbol{Q}_{k-1} - \boldsymbol{K}_k \boldsymbol{P}_{\bar{\boldsymbol{y}}_k} \boldsymbol{K}_k^T\right)\boldsymbol{H}_k^T \tag{4-10}$$

The eq.(4-10) can be further written as

$$\boldsymbol{COV}_{\boldsymbol{Z}_k^R} = \boldsymbol{R}_k - \boldsymbol{H}_k\left(\sum_{i=1}^{2N} w_i^c \left(\bar{\boldsymbol{x}}_k^{(i)} - \bar{\boldsymbol{x}}_k\right)\left(\bar{\boldsymbol{x}}_k^{(i)} - \bar{\boldsymbol{x}}_k\right)^T\right)\boldsymbol{H}_k^T - \boldsymbol{H}_k(\Phi \boldsymbol{Q}_{k-1})\boldsymbol{H}_k^T + \boldsymbol{H}_k\left(\boldsymbol{K}_k \boldsymbol{P}_{\bar{\boldsymbol{y}}_k} \boldsymbol{K}_k^T\right)\boldsymbol{H}_k^T \tag{4-11}$$

Thus, the adaptive scaling factor Φ for the system noise covariance can be determined as

$$\Phi \boldsymbol{H}_k(\boldsymbol{Q}_{k-1})\boldsymbol{H}_k^T = \boldsymbol{R}_k - \boldsymbol{H}_k\left(\sum_{i=1}^{2N} w_i^c\left(\overline{\boldsymbol{x}}_k^{(i)} - \overline{\boldsymbol{x}}_k\right)\left(\overline{\boldsymbol{x}}_k^{(i)} - \overline{\boldsymbol{x}}_k\right)^T\right)\boldsymbol{H}_k^T + \boldsymbol{H}_k\left(\boldsymbol{K}_k\boldsymbol{P}_{\bar{y}_k}\boldsymbol{K}_k^T\right)\boldsymbol{H}_k^T - \boldsymbol{COV}_{\boldsymbol{Z}_k^R} \tag{4-12}$$

Finally, the scaling factor is defined as

$$\Phi = \frac{tr(\boldsymbol{R}_k) - tr\left(\boldsymbol{H}_k\left(\sum_{i=1}^{2N} w_i^c\left(\overline{\boldsymbol{x}}_k^{(i)} - \overline{\boldsymbol{x}}_k\right)\left(\overline{\boldsymbol{x}}_k^{(i)} - \overline{\boldsymbol{x}}_k\right)^T\right)\boldsymbol{H}_k^T\right) + tr\left(\boldsymbol{H}_k\left(\boldsymbol{K}_k\boldsymbol{P}_{\bar{y}_k}\boldsymbol{K}_k^T\right)\boldsymbol{H}_k^T\right) - tr\left(\boldsymbol{COV}_{\boldsymbol{Z}_k^R}\right)}{tr(\boldsymbol{H}_k\boldsymbol{Q}_{k-1}\boldsymbol{H}_k^T)} \tag{4-13}$$

where $tr(\cdot)$ is the trace of related value

It can be seen from eq.(4-6) that the residual covariance is constructed using the information within the current window. Thus it can take into account the dynamically changing conditions of noise covariances. However, due to the limited data available within the time frame, the estimation accuracy is limited. To solve this problem, the residual covariance is further expressed into a recursive form

$$\boldsymbol{COV}_{\boldsymbol{Z}_k^R}^* = C_k\boldsymbol{COV}_{\boldsymbol{Z}_k^R} + (1 - C_k)\boldsymbol{COV}_{\boldsymbol{Z}_{k-1}^R}^* \tag{4-14}$$

where C_k is called the weighting factor, which is commonly defined by [57, 58]

$$C_k = \frac{1}{J_k} \tag{4-15}$$

where J_k is the number of the entire available epochs.

It can be seen that the state covariance described by eq.(4-14) is based on the entire available data rather than the limited data available within the time window, leading to improved accuracy. As can be seen from eq.(4-14), the state covariance is contributed by two portions. One is at current epoch, which is calculated by the windowing approximation to use the data available within the current window to characterise dynamically changing conditions being occurred. The other is at the previous epoch, which reflects the historical

tendency. The contributions at both current and previous epochs are combined via the weighting factor C_k. The state covariance takes the full contribution at the current epoch when $C_k = 1$. This covariance also takes the full contribution at the previous epoch when $C_k = 0$. The smaller value of C_k makes the current epoch smaller, and makes the previous epoch larger.

4.2.2. Modified weighting factor

In RAMIS, dynamic interaction environment is relatively stable [59], leading to a relatively small variation of noise statistics in the case without the abrupt changes, such as sudden changes, rupture events and unexpected contacts with rigid bones. However, in the case of the abrupt changes, a large variation in noise statistics will occur in a dynamic interaction environment [60]. Therefore, soft tissue characterization requires that the estimation algorithm must account for noise statistics with both of small and large variations.

However, the standard weighting factor C_k defined by eq.(4-15) cannot account for the abrupt changes occurring to the interaction with soft tissue. Figure 4-1 shows the variation of the standard weighting factor C_k in time series where an abrupt change in noise statistics is occurred at epoch t_k = 50s. As shown in Figure 4-1 (a), the C_k given by eq.(4-15) starts from the maximum value of one at the beginning. Subsequently, it decreases drastically to a small value and gradually converges to zero in time series. As the C_k stays at such a small value for most of the time, the contribution at present epoch to the residual covariance is small, but the contribution at previous epoch is large. Due to the small contribution at

present epoch in most of the time, the residual covariance is unable to account for the abrupt changes in the system noise statistics. As shown in Figure 4-1 (a), as the C_k still remains at the small value at epoch t_k = 50s, it leads to the failure to account for the abrupt change of noise statistics being occurred at this time. Accordingly, the C_k given by eq.(4-15) is only valid to the case that system noise statistics are constant or have a small variation, making the proposed Adaptive UKF unable to account for the dynamically changing conditions.

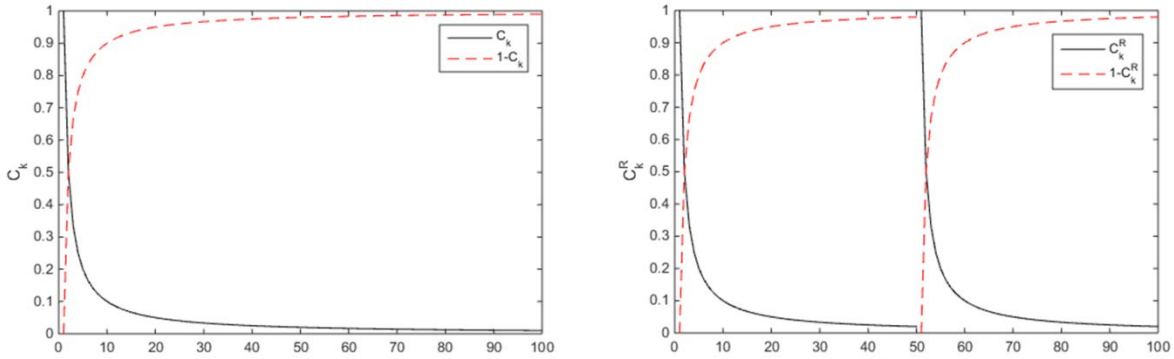

(a) Standard weighting factor (b) Modified weighting factor

Figure 4-1 The standard weighting factor (a) and modified weighting factor (b), where an abrupt change occurs at time point t_k = 50s: The black solid line represents the proportion of the current variation of residual covariance while the red dash line the previous estimation of residual covariance

In order to accommodate large variations in noise statistics, the standard weighting factor C_k defined by eq.(4-15) is modified as

$$C_k^R = \frac{1}{(J_k - b)} \tag{4-16}$$

$$b = (k_r - 1)g(k - k_r) \tag{4-17}$$

where $g(\cdot)$ is a unit step function, and k_r is the index of the epoch where an abrupt change occurs. An abrupt change can be identified by the detecting algorithm [27, 36].

The initial value of the parameter *b* is zero. When an abrupt change occurs at current epoch, the parameter *b* will be updated to $k_r - 1$, making the C_k^R become one again. Consequently, system noise covariance estimation, the residual covariance is calculated by taking full contribution at present epoch to account for the abrupt change. Figure 4-1 (b) shows the variation of the modified weighting factor C_k^R where an abrupt change in the system noise statistics occurred at epoch t_k = 50s. Similar to the C_k, the C_k^R starts from the maximum value of one, the residual covariance takes the full contribution at the present epoch. Subsequently, the C_k^R value drops drastically and remains at a small value until an abrupt change occurs. With such a small value of the C_k^R, the residual covariance follows the one at previous epoch for a small variation in system noise covariance. When the abrupt change occurs at time point *k* = 50s ($k_r = 50$s), the parameter *b* defined by eq.(4-17) will be updated to $k_r - 1$, restoring the C_k^R back to the maximum value of one to account for the abrupt change. Subsequently, the C_k^R drastically drops to and stays at a small value until a new abrupt change occurs. This variation process of the C_k^R repeats whenever an abrupt change occurs, the system noise covariance can be adjusted to account for an abrupt change by taking the full contribution at present epoch.

By modifying the weighting factor, eq.(4-14) becomes

$$\boldsymbol{COV}^{*}_{\boldsymbol{Z}^{R}_{k}} = C^{R}_{k}\boldsymbol{COV}_{\boldsymbol{Z}^{R}_{k}} + (1 - C^{R}_{k})\boldsymbol{COV}^{*}_{\boldsymbol{Z}^{R}_{k-1}} \tag{4-18}$$

Thus, the adaptive scaling factor is calculated by

$$\Phi = \frac{tr(\boldsymbol{R}_k) - \ tr\left(\boldsymbol{H}_k\left(\sum_{i=1}^{2N} w_i^c\left(\overline{\boldsymbol{x}}_k^{(i)} - \overline{\boldsymbol{x}}_k\right)\left(\overline{\boldsymbol{x}}_k^{(i)} - \overline{\boldsymbol{x}}_k\right)^T\right)\boldsymbol{H}_k^T\right) - tr\left(\boldsymbol{H}_k\left(\boldsymbol{K}_k\boldsymbol{P}_{\overline{\boldsymbol{y}}_k}\boldsymbol{K}_k^T\right)\boldsymbol{H}_k^T\right) - tr\left(\boldsymbol{COV}^{*}_{\boldsymbol{Z}^{R}_{k}}\right)}{tr(\boldsymbol{H}_k\boldsymbol{Q}_{k-1}\boldsymbol{H}_k^T)} \tag{4-19}$$

4.2.3. Estimation of measurement noise covariance

The measurement noise covariance can also be estimated in the same way as the system noise covariance. By introducing an adaptive scaling factor Γ, the measurement noise covariance can be represented as

$$\boldsymbol{R}_k = \Gamma\boldsymbol{R}_{k-1} \tag{4-20}$$

Substituting eq.(4-20) into eq.(3-17), the predicted measurement covariance can be further written as modified predicted measurement covariance $\boldsymbol{P}^{m}_{\overline{\boldsymbol{y}}_k}$

$$\boldsymbol{P}^{m}_{\overline{\boldsymbol{y}}_k} = \sum_{i=1}^{2N} w_i^c\left(\overline{\boldsymbol{y}}_k^{(i)} - \overline{\boldsymbol{y}}_k\right)\left(\overline{\boldsymbol{y}}_k^{(i)} - \overline{\boldsymbol{y}}_k\right)^T + \Gamma\boldsymbol{R}_{k-1} \tag{4-21}$$

It can be seen from eq.(4-21) that the measurement noise covariance can be adjusted via the adaptive scaling factor Γ.

Denote the innovation vector $\boldsymbol{Z}_k^I$ as

$$\boldsymbol{Z}_k^I = \boldsymbol{y}_k - \overline{\boldsymbol{y}}_k \tag{4-22}$$

Using the windowing approximation [56], the innovation covariance can be directly calculated with the innovation vector $\boldsymbol{Z}_k^I$

$$\boldsymbol{COV}_{\boldsymbol{Z}_k^I} = \frac{1}{m}\sum_{j=1}^{m} \boldsymbol{Z}_{k-j}^I \boldsymbol{Z}_{k-j}^{I\,T} \tag{4-23}$$

Similar to eq.(4-18), the actual measurement covariance $\boldsymbol{COV}_{\boldsymbol{Z}_k^I}$ can be further expressed by a recursive form as

$$\boldsymbol{COV}^*_{\boldsymbol{Z}_k^I} = C_k^R \boldsymbol{COV}_{\boldsymbol{Z}_k^I} + (1 - C_k^R)\boldsymbol{COV}^*_{\boldsymbol{Z}_{k-1}^I} \tag{4-24}$$

where the modified weighting factor C_k^R is also applied to deal with both small and large variations in the measurement noise covariance.

By matching the modified predicted measurement covariance given by the innovation covariance in eq.(4-21), we readily have

$$\sum_{i=1}^{2N} w_i^c \left(\overline{\boldsymbol{y}}_k^{(i)} - \overline{\boldsymbol{y}}_k\right)\left(\overline{\boldsymbol{y}}_k^{(i)} - \overline{\boldsymbol{y}}_k\right)^T + \Gamma \boldsymbol{R}_{k-1} = \boldsymbol{COV}^*_{\boldsymbol{Z}_k^I} \tag{4-25}$$

From eq.(4-25), the adaptive scaling factor Γ for estimation of measurement noise covariance is determined as

$$\Gamma = \frac{tr\left(\boldsymbol{COV}^*_{\boldsymbol{Z}_k^I}\right) - tr\left(\sum_{i=1}^{2N} w_i^c \left(\overline{\boldsymbol{y}}_k^{(i)} - \overline{\boldsymbol{y}}_k\right)\left(\overline{\boldsymbol{y}}_k^{(i)} - \overline{\boldsymbol{y}}_k\right)^T\right)}{tr(\boldsymbol{R}_{k-1})} \tag{4-26}$$

4.3. Performance evaluation and discussions

A prototype system was implemented using the proposed method for online soft tissue characterization. This system employed measurements of interaction force and displacement as inputs to estimate the nonlinear parameters of the H-C model. Based on the estimated parameters of the H-C model, the interaction force data with soft tissue were reconstructed from displacements. Subsequently, the reconstructed forces were compared with the interaction forces to calculate the estimation error. The simulations, the experiments, and the comparison analyses were conducted to evaluate the performance of the proposed approach comprehensively in terms of: (i) system noise covariance estimation; (ii) measurement noise covariance estimation; (iii) the effect of the weighting factor; and (iv) the force reconstruction based on the estimated parameters of the H-C model.

4.3.1. Simulations and analysis

Simulations were conducted to comprehensively evaluate the performance of the proposed solution in estimating system and measurement noise covariances together with the associated force reconstructions. The time step for the simulations was set to 10ms. The initial state was defined as $\boldsymbol{x}_0$= [0.1, 0.1, 0.01, 0.0001, 0.0001, 1, 1].

4.3.1.1. *System noise covariance estimation*

For the performance evaluation in terms of system noise covariance estimation, it is supposed that the measurement noise statistics is completely known. Without loss of generality, set $\boldsymbol{R}_k = 1$ and $E(\boldsymbol{r}_k) = 0$. Two cases were studied. The first case was that the system noise covariance is constant or has a small variation. The other case was that the system noise covariance involves abrupt changes.

4.3.1.1.1. Constant or small-variation system noise covariance

Simulation trials were conducted under the same conditions by the Adaptive UKF (AUKF) and Recursive Adaptive UKF (RAUKF) for the case that the system noise covariance is constant or has a small variation. The measurement data were obtained from the H-C model by adding white Gaussian noise with zero mean and the covariance of 0.036N. The initial estimation value was $\widehat{\boldsymbol{Q}}_0$ = 0.004N, the window size was *m* = 4, the real covariance of system noise was $\boldsymbol{Q}_k$ = 0.036N, and $E(\boldsymbol{q}_k)$ = 0. The simulation time was 90s. As shown in Figure 4-2, the system noise covariance estimated by AUKF via the windowing approximation involves large oscillations during the simulation. This is because the limited data available within the small window lead to poor estimation accuracy. In contrast, the system noise covariance estimated by RAUKF via the recursion method is close to the real value after 20s. This is because the estimation via the recursion method is obtained based on the entire available data. The RMSE (Root Mean Square Error) of AUKF is 0.0125N, while after 20s the RMSE of RAUKF is 0.0032N. It should be noted that in the estimation results of RAUKF are the same under both standard and modified weighting factors for this trial case.

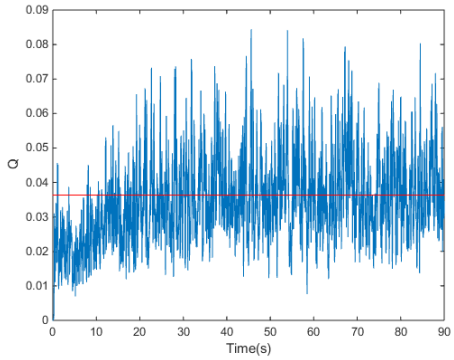

(a) AUKF via windowing approximation

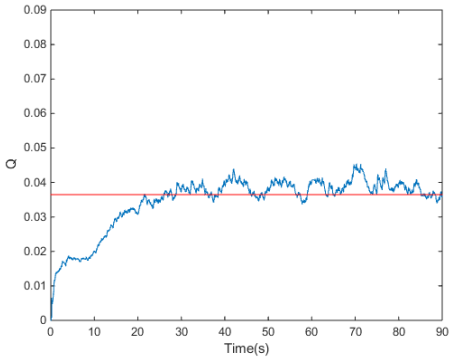

(b) RAUKF via recursion

Figure 4-2 Estimations of system noise covariance by both of AUKF and RAUKF for the case that system noise covariance is constant or in a small variation: The estimated system noise covariances are indicated by the blue line and the reference values are indicated by the red line

Under the estimated system noise covariances in Figure 4-2, Figure 4-3 illustrates the estimation errors in terms of the force reconstruction by both AUKF and RAUKF. It is clear that the estimation error of RAUKF is much smaller than that of AUKF. Since the system noise covariance estimated by AUKF involves large oscillations during the simulation, the resultant estimation error also involves large oscillations during the entire simulation time. In contrast, since the system noise covariance estimated by RAUKF is close to the true value after the initial time period of 20s, the resultant estimation error becomes small and is further converged since then. The largest estimation error is 0.0394N for RAUKF, but 0.1853N for AUKF. The mean estimation error of AUKF is 0.0374N when RAUKF is 0.0053N. The RMSE of RAUKF is 0.0070N, while that of AUKF is almost nine times larger, which is 0.0475N. Table 4-1 summarises the estimation errors via AUKF and RAUKF.

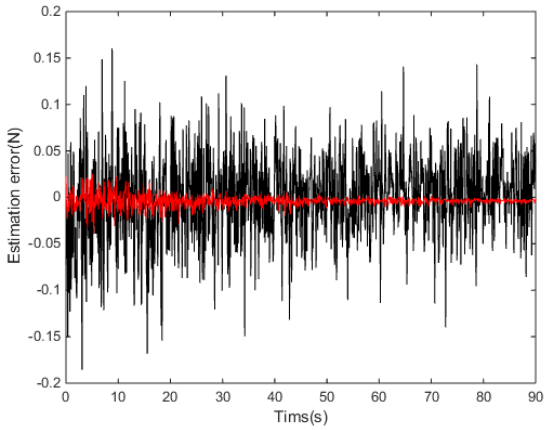

Figure 4-3 Estimation errors in force reconstruction by both of AUKF and RAUKF corresponding to the estimated system noise covariances as shown in Figure 4-2: The estimation error of AUKF is indicated by the black line and that of RAUKF is indicated by the red line

Table 4-1 Estimation errors of AUKF and RAUKF in the case that system noise covariance is constant or has a small variation

Errors(N)	**AUKF**	**RAUKF**
Mean error	0.0374	0.0053
Max error	0.1853	0.0394
RMSE	0.0475	0.0070

4.3.1.1.2.System noise covariance involving abrupt changes

To analyse the effect of the weighting factor on system noise covariance estimation, simulation trials were conducted under the same conditions by RAUKF via both standard and modified weighting factors for the case of system noise covariance involving abrupt changes. The input signals were obtained from the H-C model by adding white Gaussian noise with zero mean. The noise covariance was set to 0.036N within [0, 36s] and 0.576N within (36s, 70s], leading to an abrupt change from 0.036N to 0.576N at 36s. The initial estimation value was $\widehat{\boldsymbol{Q}}_0 = 0.004$N, the window size was set to $m = 14$, and the simulation time was 70s.

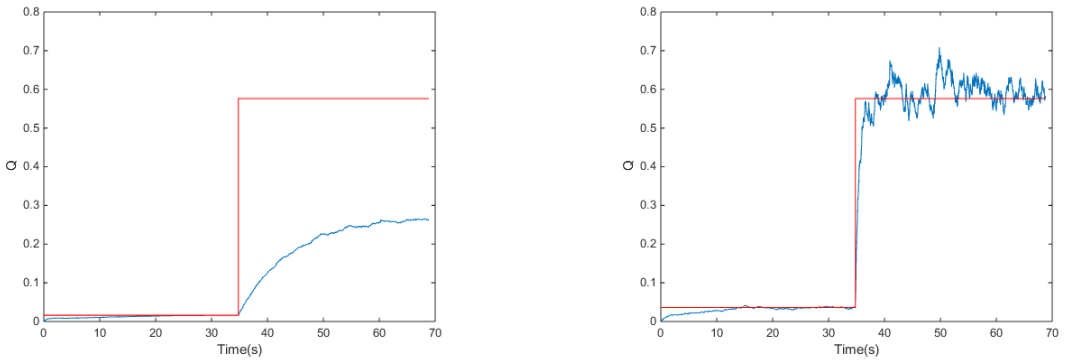

(a) RAUKF with the standard weighting factor (b) RAUKF with the modified weighting factor

Figure 4-4 Estimations of system noise covariance by RAUKF with both of standard and modified weighting factors for the case that system noise covariance involves abrupt changes: The estimated system noise covariances are indicated by the blue line, and the reference values are indicated by red line

Figure 4-4 shows the system noise covariances estimated by RAUKF via both standard and modified weighting factors. Although the estimation results with both weighting factors follow the reference value of 0.036N within [0, 36s], the estimation of the standard

weighting factor does not follow the abrupt change from 0.036N to 0.576N at 36s, leading to the mean error of 0.372N after 36s. In contrast, the estimation of system noise covariance under the modified weighting factor rapidly follows the abrupt change from 0.036N to 0.576N at 36s, leading to the mean error of 0.0088N after 36s. This demonstrates that RAUKF can accommodate abrupt changes in system noise covariance with the modified weighting factor.

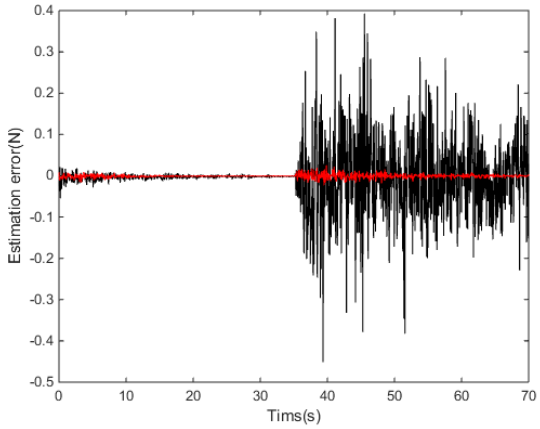

Figure 4-5 Estimation errors in terms of force reconstruction by RAUKF corresponding to the estimated system noise covariances via both standard and modified weighting factors as shown in Figure 4-4: The estimation error via the standard weighting factor is indicated by the black line, and the one via the modified weighting factor is indicated by the red line

Figure 4-5 shows the estimation errors in force reconstruction under the estimated system noise covariances as shown in Figure 4-4. It can be seen that before 36s although the RAUKF estimation errors via both standard and modified weighting factors are small and converged to zero, the one via the modified weighting factor is even smaller and has a faster convergence speed. However, after 36s, due to the biased estimate of the system noise

covariance, the estimation error by RAUKF via the standard weighting factor involves large oscillations, leading to the RMSE of 0.0749N. In contrast, the estimation error by RAUKF via the modified weighting factor is much smaller and converged to zero, leading to the RMSE of 0.0046N. This demonstrates that the modified weighting factor enables the RAUKF to account for abrupt changes in system noise covariance, thus leading to improved estimation accuracy. Table 4-2 summarizes the RAUKF estimation errors via both standard and modified weighting factors.

Table 4-2 RAUKF estimation errors under both standard and modified weighting factors for the case that system noise covariance involves abrupt changes

Errors (N)	Standard weighting factor	Modified weighting factor
Mean error	0.0030	0.0009
Max error	0.4517	0.0389
RMSE	0.0749	0.0046

4.3.1.2. *Measurement noise covariance estimation*

In order to evaluate the estimation of measurement noise covariance, it is assumed that the system noise statistics are exactly known. Without loss of generality, choose $\boldsymbol{Q}_k = 1$ and $E(\boldsymbol{q}_k) = 0$. Similar to Section 4.3.1.1, two cases were studied. The first case was when the measurement noise covariance is constant or in a small variation, and the other was the measurement noise covariance involves abrupt changes.

4.3.1.2.1.Constant or small-variation measurement noise covariance

Simulation trials were conducted under the condition that the measurement noise covariance is constant or has a small variation by both AUKF and RAUKF. It should be noted that in this case, the RAUKF estimation results are the same under both standard and modified weighting factors.

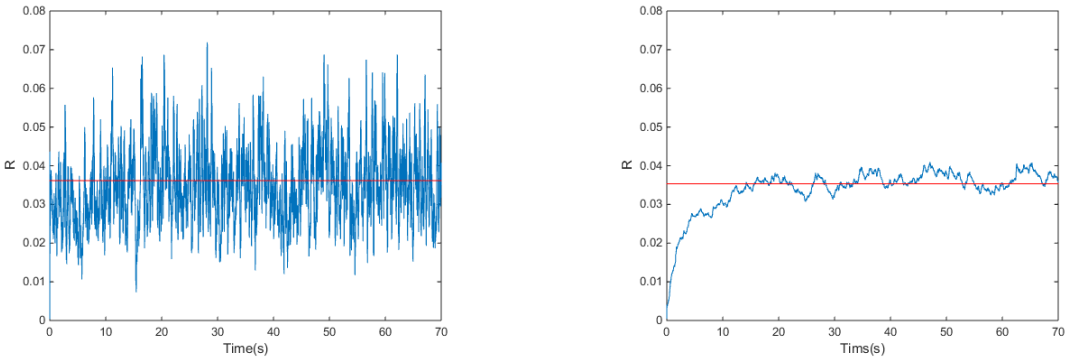

(a) AUKF via windowing approximation (b) RAUKF via recursion

Figure 4-6 Estimations of measurement noise covariance by both of AUKF and RAUKF for the case that measurement noise covariance is constant or small-variation: The estimated measurement noise covariances are indicated by the blue line and the reference values are indicated by the red line

The input signals were obtained from the H-C model by adding white Gaussian noise with zero mean and the covariance of 0.036N. The initial estimation value was $\widehat{\boldsymbol{R}}_0 = 0.004\text{N}$. The window size was set to m = 4. The simulation time was 70s. As shown in Figure 4-6, the estimation of measurement noise covariance, by AUKF via the windowing approximation, involves the large oscillations during the entire testing time, while the one by RAUKF via recursion is very close to the reference value after 15s. The RMSE of RAUKF is 0.0051N, which is almost two times smaller than the AUKF with RMSE of 0.0101N. This demonstrates the accuracy of RAUKF is significantly higher than that of AUKF for estimation of measurement noise covariance.

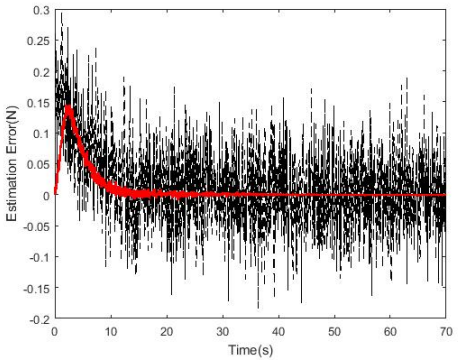

Figure 4-7 Estimation errors in force reconstruction by both of AUKF and RAUKF corresponding to the estimated measurement noise covariances as shown in Figure 4-6: The estimation error by AUKF is indicated by the black line and that by RAUKF is indicated by the red line

Figure 4-7 illustrates the estimation errors in the force reconstruction by both AUKF and RAUKF under the estimated measurement noise covariances as shown in Figure 4-6. It can be seen clearly that the estimation error of AUKF is much larger than that of RAUKF during the entire testing time. In addition, the estimation error of RAUKF is converged close to zero after 15s while that of AUKF becomes slightly smaller than initial estimation error. This is because the estimated measurement noise covariance by windowing approximation fluctuates during the entire simulation while that by RAUKF is converged close to the reference value. The RMSE of RAUKF is 0.0286N, which is two-three times smaller than that of AUKF (0.0708N). Further, the maximum and mean estimation errors of AUKF are about two times larger than those of RAUKF. The maximum estimation error is 0.2905N for AUKF, while the error is 0.145N for RAUKF. The mean estimation error is 0.0551N for AUKF, while the error is 0.0102N for RAUKF. Therefore, the estimation accuracy of RAUKF is significantly

higher than that of AUKF. Table 4-3 compares the estimation errors by both AUKF and RAUKF.

Table 4-3 Estimation errors of AUKF and RAUKF for constant or small-variation measurement noise covariance

Errors (N)	AUKF	RAUKF
Mean error	0.0551	0.0102
Max error	0.2950	0.1450
RMSE	0.0708	0.0286

4.3.1.2.2. Measurement noise covariance involving abrupt changes

To analyse the effect of the weighting factor for measurement noise covariance estimation, trials were conducted under the same conditions by RAUKF via both standard and modified weighting factors for the case of measurement noise covariance involving abrupt changes. The input signals were obtained from the H-C model by adding white Gaussian noise with zero mean. The covariance of this measurement noise was set to 0.036N within [0, 32s] and 0.576N within (32s, 70s], leading to an abrupt change at 32s. The initial estimation value was $\widehat{\boldsymbol{R}}_0$ =0.004N. The window size *m* = 14. The simulation time was 70s. Figure 4-8 shows the system noise covariances estimated by RAUKF via both standard weighting factor and modified weighting factor. As shown in Figure 4-8, the estimations of measurement noise covariance under both weighting factors follow the reference value of 0.036N within [0, 32s]. However, the estimation under the standard weighting factor does not follow the abrupt change from 0.036N to 0.576N at 32s, leading to the large mean error of 0.2662N after 32s.

In contrast, the estimation under the modified weighting factor follows closely the abrupt change, leading to the mean error of 0.043N after 32s.

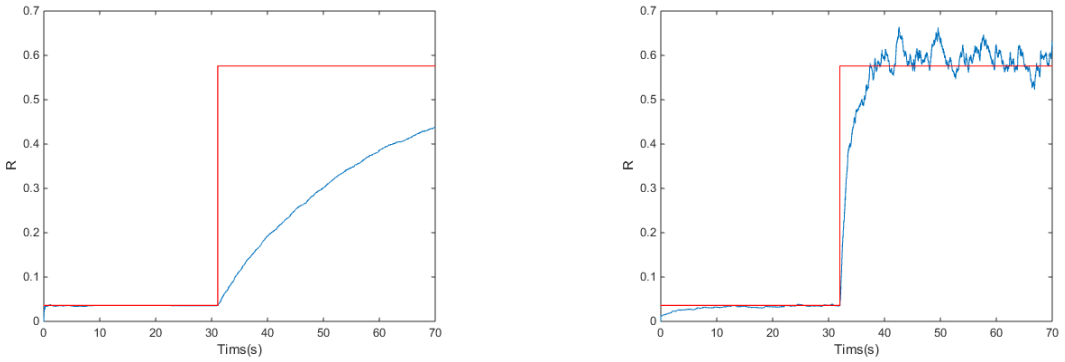

(a) RAUKF with the standard weighting factor (b) RAUKF with the modified weighting factor

Figure 4-8 Measurement noise covariance estimations by RAUKF via both standard and modified weighting factors for the case that measurement noise covariance involves abrupt changes: The estimated measurement noise covariances are indicated by the blue line and the reference values are indicated by the red line

Figure 4-9 shows the estimation errors in force reconstruction corresponding to the estimated measurement noise covariances as shown in Figure 4-8. Within the time period [0, 32s] before the abrupt change at 32s, both standard and modified weighting factors result in the similar estimation error. The mean error is 0.0025N by the standard weighting factor, and 0.0023N by the modified weighting factor. However, after the abrupt change at 32s, due to the biased estimate of the measurement noise covariance, the use of the standard weighting factor results in a large magnitude of oscillations in the estimation error curve, leading to the RMSE of 0.0907N. In contrast, with the modified weighting factor, the magnitude of oscillations in the estimation error curve after 32s is significantly decreased and gradually converged to zero, leading to the RMSE of 0.0444N. The results proved that with the modified weighting factor, RAUKF is able to accommodate abrupt changes in the

measurement noise covariance. Table 4-4 lists the estimation errors of RAUKF under both standard and modified weighting factor, where the mean error and maximum error under the standard weighting factor are 0.0603N and 0.5493N, while 0.0284N and 0.2961N under the modified weighting factor.

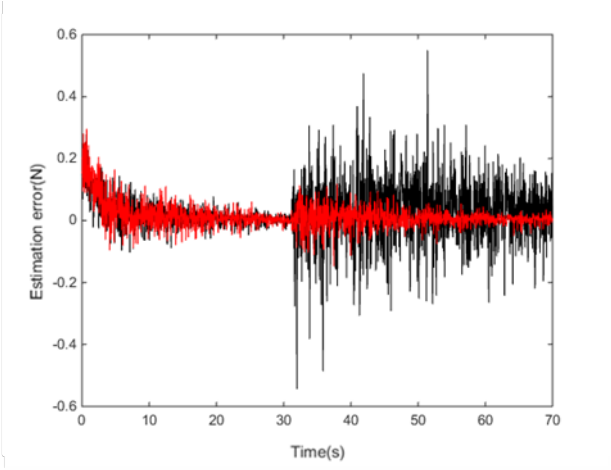

Figure 4-9 Estimation errors in force reconstruction by RAUKF corresponding to the estimated measurement noise covariances via both standard and modified weighting factors as shown in Figure 4-8: The estimation error via the standard weighting factor is indicated by the black line, and the one via the modified weighting factor is indicated by the red line

Table 4-4 Estimation errors of RAUKF via both standard and modified weighting factors

Errors (N)	Standard weighting factor	Modified weighting factor
Mean error	0.0603	0.0284
Max error	0.5493	0.2961
RMSE	0.0907	0.0444

4.3.2. Experiments and analysis

The performance evaluation is also conducted on two experimental cases in the presence of abrupt changes. One was for robotic-assisted needle insertion in the presence of rapture events, where the measurement data were acquired from the literature. The other was for mechanical indentation in the presence of sudden changes.

4.3.2.1. *Robotic-assisted needle insertion*

Trials were conducted to evaluate the performance of the proposed methodology for the case of robotic-assisted needle insertion. The experimental data of interaction force and displacement during the process of needle insertion were obtained from the literature [55] as shown in Figure 4-10. The inserted needle penetrated the soft tissue layers (L1, L2, L3, L4 and L5) in sequence. The penetrations caused the abrupt changes in force signal as shown in Figure 4-10 (Rupture L1, L2, L3, L4 and L5).

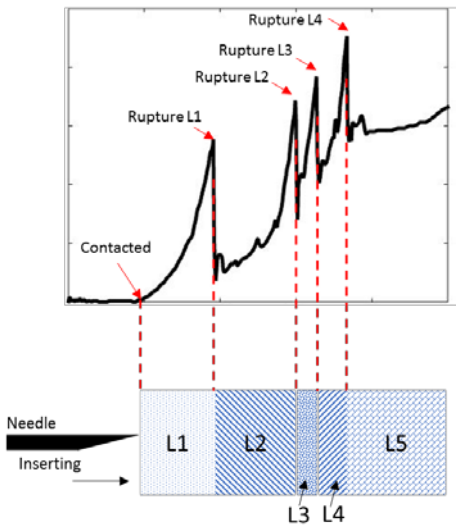

Figure 4-10 The measured interaction force when the needle is inserted into heterogeneous materials

The interaction force consists of the four cusps where are at the displacements of around 20mm, 29mm, 32mm, and 36mm (see Figure 4-11). These cusps represent the rupture

events encountered by the robotic needle during the insertion process. For comparison analysis, trials were conducted under the same conditions by three different methods: UKF, AUKF, and RAUKF with the modified weighting factor. The initial state and noise covariance were set as $\boldsymbol{x}_0$= [0.1, 0.1, 0.01, 0.0001, 0.0001, 1, 1], $\boldsymbol{Q}_0$= 0.1 and $\boldsymbol{R}_0$= 0.1. The window size for both AUKF and RAUKF was set to *m* =4.

Figure 4-11 shows the reconstructed forces with the estimated parameters of the H-C model by UKF, AUKF, and RAUKF, respectively. It can be seen that the UKF estimation results in large errors at the four cusps, where the estimation error 0.378N at the first cusp of around 20mm is most significant. An obvious deviation is also stayed in the displacement range from around 40mm to 50mm after the four cusp, leading to the mean error of 0.068N and the RMSE of 0.15N.

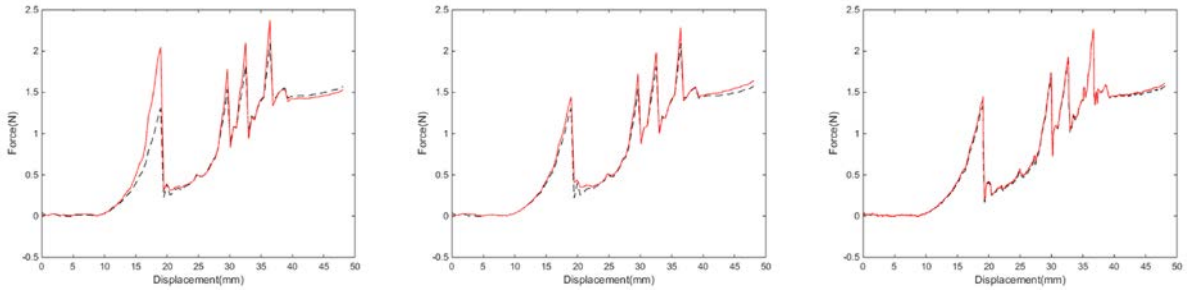

(a)UKF (b)AUKF (c)RAUKF

Figure 4-11 Reconstructed forces by UKF, AUKF, and RAUKF: The interaction forces are indicated by the black dash line and the reconstructed forces the red solid line

It also can be seen that AUKF improves the estimation accuracy of UKF at the four cusps, leading to the mean error of 0.044N and RMSE of 0.069N. However, the pronounced errors still exist at and after the four cusps. This is because the estimated noise covariance in AUKF

is inaccurate as shown in the previous simulations. In contrast, the reconstructed forces by RAUKF are very close to the reference values at and after the four cusps, leading to the mean error of 0.020N and RMSE of 0.039N.

Table 4-5 lists the mean and maximum errors as well as RMSEs of the three methods. It can be seen that although both AUKF and RAUKF outperform UKF, RAUKF has the smallest estimation errors of 0.02N and RMSE of 0.039N. The mean and maximum errors of RAUKF are more than three times smaller than those of UKF. The RMSE of RAUKF is almost four times smaller than that of UKF. The mean and maximum errors as well as RMSE of RAUKF are also much smaller than those of AUKF.

Table 4-5 Estimation errors of UKF, AUKF, and RAUKF for the case of robotic-assisted needle insertion

Error (N)	**UKF**	**AUKF**	**RAUKF**
Mean Error	0.683	0.044	0.020
Maximum Error	0.738	0.346	0.205
RMSE	0.150	0.069	0.039

4.3.2.2. *Mechanical indentation with sudden changes*

Mechanical indentation tests were also conducted to evaluate the performance of the proposed method for soft tissue characterization in the presence of sudden changes. The indentation tests were conducted on a phantom tissue sample using the DMA (Dynamic Mechanical Analyser, Seiko Instruments). As shown in Figure 4-12, the phantom tissue is made up of silicone rubbers, which have the similar characteristics as human soft tissue [61]. The phantom tissue was of cubic shape (1cm × 1cm × 0.55cm) to fit into the DMA machine. An indenter of 1cm diameter was used to compress the phantom tissue vertically. In order to present sudden changes, the indenter was controlled to compress the phantom tissue with a given displacement and then hold at the displacement for around 0.9s. The shape of silicon cube was abruptly deformed when the displacement of the indenter was increased dramatically, leading the sudden changes. Subsequently, the indenter was controlled at the maximum speed (1,000,000 um/min) to increase the displacement by 1mm and then hold at the new displacement for around 0.9s, with the conduction of three times. The data of displacement and load were acquired from the DMA during the compression tests. As shown in Figure 4-13, there were three abrupt changes (three steps) in the force curve at around 0.9s. 1.8s and 2.7s, which represent sudden changes in RAMIS. Trials were conducted under the same conditions by UKF, AUKF, and RAUKF based on measured forces and displacements. The parameters used in these filters were the same as the previous case of robotic-assisted needle insertion.

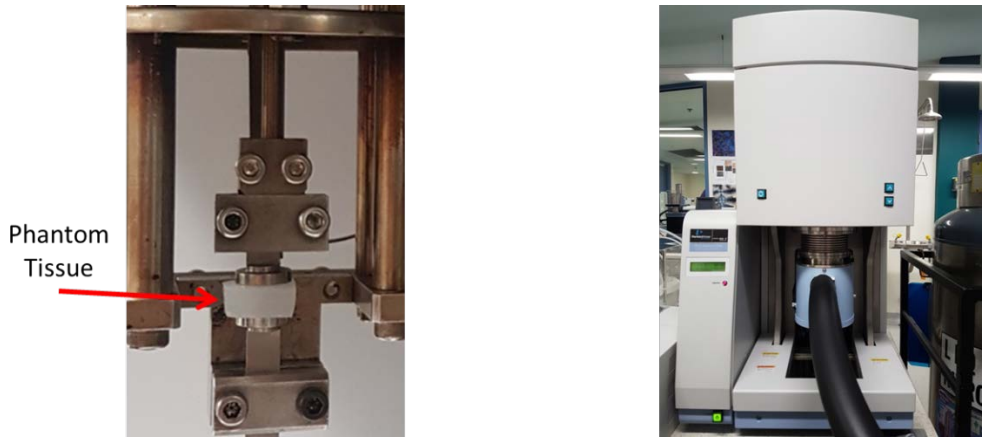

(a) (b)

Figure 4-12 Experimental setups for mechanical indentation on the phantom tissue: (a) the indenter and phantom tissue; and (b) the appearance of DMA

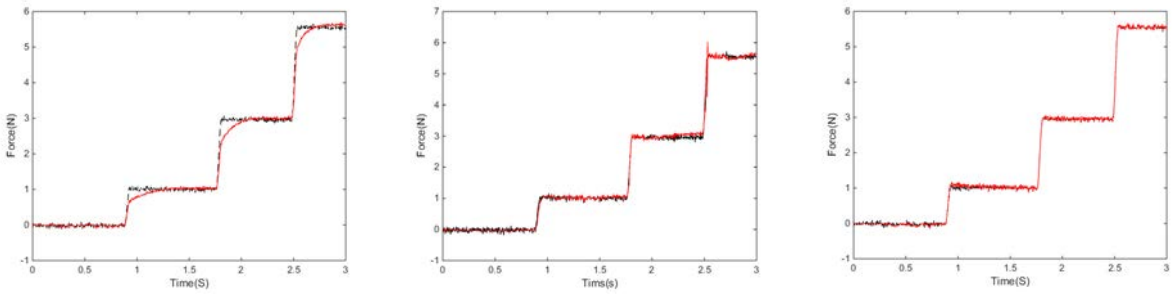

(a) UKF (b) AUKF (c) RAUKF

Figure 4-13 Reconstructed forces by UKF, AUKF, and RAUKF for the case of mechanical indentation: The interaction forces are indicated by the black dash line and the reconstructed forces the red solid line

Figure 4-13 shows the reconstructed forces by UKF, AUKF, and RAUKF from measured forces and displacements. It can be seen that the UKF estimation has large estimation errors at each abrupt change, leading to the maximum error of 0.6341N, mean error of 0.0099N and RMSE of 0.0157N, respectively. Comparing to the UKF estimation, the AUKF estimation follows the reference force curve, without involving a large estimation error. The mean error of AUKF is 0.0064N, which is smaller than that of UKF. However, due to the inaccurate

noise covariance estimation, the AUKF estimation error becomes large after around 2s with a large peak error at 2.5s where the interaction force is changed abruptly. Different from UKF and AUKF, due to the use of the modified weighting factor, the RAUKF estimation closely follows the reference force curve, especially at the three abrupt changes. Its RMSE is 0.0098N, which is much smaller than those of UKF and AUKF.

Table 4-6 Estimation errors of UKF, AUKF, and RAUKF for the case of mechanical indentation with sudden changes

Error(N)	UKF	AUKF	RAUKF
Mean Error	0.0099	0.0064	0.0062
Maximum Error	0.6341	0.0727	0.0638
RMSE	0.0157	0.0109	0.0098

Table 4-6 compares the estimation errors of the three methods. It can be seen that in addition to the mean error, the maximum error and RMSE of RAUKF are also much smaller than those of UKF and AUKF.

4.4. Summary

This chapter presents a new nonlinear filtering approach for online nonlinear soft tissue characterization in RAMIS. An adaptive UKF was established based on the nonlinear H-C model for online estimate soft tissue parameters without prior knowledge of noise statistics. A recursive adaptive UKF with the modified weighting factor was further developed to

improve the estimation accuracy and accommodate large variations in noise statistics. The comparison in the simulations and experiments demonstrated that the proposed methodology can effectively estimate soft tissue parameters under the system and measurement noises in both small and large variations, leading to the improved filtering accuracy and robustness in comparison with the UKF-based method.

5. Random weighting strong tracking unscented Kalman filter in the presence of model error

5.1. Introduction

The proposed RAUKF in Chapter 4 addresses the problem of inaccurate noise statistics in UKF for online soft tissue characterization method. However, the UKF also requires an accurate system model. In RAMIS, the system model always involves uncertainties such as inappropriate initial conditions, modelling error due to model simplification for the purpose of computational efficiency, unexpected system noises and stochastic drifts. These uncertainties deteriorate UKF-based solutions.

To solve the model error problem in the UKF-based online soft tissue characterization, this chapter presents a random weighting strong tracking unscented Kalman filter (RWSTUKF). This RWSTUKF adopts the Strong Tracking (ST) method to address the UKF problem of performance degradation due to system model error. A scaling factor is introduced into the predicted state covariance to account for a system model error. To prevent the cumbersome calculation of Jacobian matrix of contact model, this scaling factor is determined according to the orthogonality principle, where the random weighting concept is adopted to provide the reliable estimation for innovation covariance. Simulations and comparison analysis with UKF were conducted to comprehensively evaluate the performance of the proposed RWSTUKF.

The random weighing concept was proposed to improve the estimation performance of windowing approximation method [62, 63]. Assume a distribution function $A(x)$ and independent and identical distributed stochastic variable $X_1, \dots, X_n$ based on the $A(x)$, the empirical distributed function is established as

$$A_n(x) = \frac{1}{n}\sum_{i=1}^{n} I_{(X_i \le x)} \tag{5-1}$$

where $I_{(X_i \le x)}$ is the indicator function. The distribution function in (5-1) could be re-written with the random vector $v_1, \dots, v_n$ as

$$V_n(x) = \sum_{i=1}^{n} v_i I_{(X_i \le x)} \tag{5-2}$$

Note that the random vector v_n should be meet the condition of Dirichlet distribution $D\ (1,1,\dots,1)$, which is represented as $\sum_{i=1}^{n} v_i = 1$ and the joint density function $j(v_1, v_2, \dots, v_3) = \Lambda(n)$ where $(v_1, v_2, \dots, v_n) \in D_n$ and $D_{n-1} = [(v_1, v_2, \dots, v_{n-1}): v_k \geq 0, k = 1,2 \dots, n-1, \sum_{k=1}^{n-1} v_k \leq 1]$.

5.2. Analysis of the effect of an inaccurate system model in UKF

The predicted state in eq.(3-14) can be rewritten as

$$\bar{\boldsymbol{x}}_k = \frac{1}{2N}\sum_{i=1}^{2N} \boldsymbol{w}_i^m \left(f(\bar{\boldsymbol{x}}_{k-1}^{(i)})\right) \tag{5-3}$$

Consider the contact state equation eq.(3-9) has the error $f_e(\cdot)$. The state prediction error $\breve{\boldsymbol{x}}_k$ can be calculated as

$$\breve{\boldsymbol{x}}_k = \frac{1}{2N}\sum_{i=1}^{2N} \boldsymbol{w}_i^m \, f_e\left(\bar{\boldsymbol{x}}_{k-1}^{(i)}\right) \tag{5-4}$$

The eq.(5-4) represents a predicted state in the presence of model error $f_e(\cdot)$.

Summing eq.(5-3) and eq.(5-4) together yields

$$\bar{\boldsymbol{x}}_k + \breve{\boldsymbol{x}}_k = \frac{1}{2N}\sum_{i=1}^{2N} \boldsymbol{w}_i^m \left(f(\bar{\boldsymbol{x}}_{k-1}^{(i)})\right) + \frac{1}{2N}\sum_{i=1}^{2N} \boldsymbol{w}_i^m \, f_e\left(\bar{\boldsymbol{x}}_{k-1}^{(i)}\right) \tag{5-5}$$

eq.(5-5) represents a predicted state in the presence of model error $f_e(\cdot)$.

The predicted state covariance in the presence of model error $f_e(\cdot)$ is calculated with eq.(5-5) by unscented transformation (UT) method as

$$\sum_{i=1}^{2N} \boldsymbol{w}_i^c \left(\bar{\boldsymbol{x}}_k^{(i)} - \bar{\boldsymbol{x}}_k + \breve{\boldsymbol{x}}_k^{(i)} - \breve{\boldsymbol{x}}_k\right)\left(\bar{\boldsymbol{x}}_k^{(i)} - \bar{\boldsymbol{x}}_k + \breve{\boldsymbol{x}}_k^{(i)} - \breve{\boldsymbol{x}}_k\right)^T + \boldsymbol{Q}_k \tag{5-6}$$

where $\breve{\boldsymbol{x}}_k^{(i)}$, $\bar{\boldsymbol{x}}_k^{(i)}$ are the sigma points, which are selected from $\breve{\boldsymbol{x}}_k$ and $\bar{\boldsymbol{x}}_k$ respectively.

Denote

$$\begin{aligned} \bar{\boldsymbol{X}}_k^{(i)} &= \bar{\boldsymbol{x}}_k^{(i)} - \bar{\boldsymbol{x}}_k \\ \breve{\boldsymbol{X}}_k^{(i)} &= \breve{\boldsymbol{x}}_k^{(i)} - \breve{\boldsymbol{x}}_k \end{aligned} \tag{5-7}$$

eq.(5-6) can be further written with eq.(5-7) as

$$\sum_{i=1}^{2N} \boldsymbol{w}_i^c \left(\bar{\boldsymbol{X}}_k^{(i)} + \breve{\boldsymbol{X}}_k^{(i)}\right)\left(\bar{\boldsymbol{X}}_k^{(i)} + \breve{\boldsymbol{X}}_k^{(i)}\right)^T + \boldsymbol{Q}_k \tag{5-8}$$

$$= \sum_{i=1}^{2N} \boldsymbol{w}_i^c \left(\bar{\boldsymbol{X}}_k^{(i)}\bar{\boldsymbol{X}}_k^{(i)^T} + \bar{\boldsymbol{X}}_k^{(i)}\breve{\boldsymbol{X}}_k^{(i)} + \breve{\boldsymbol{X}}_k^{(i)}\bar{\boldsymbol{X}}_k^{(i)^T} + \breve{\boldsymbol{X}}_k^{(i)}\breve{\boldsymbol{X}}_k^{(i)^T}\right) + \boldsymbol{Q}_k$$

Define the predicted state covariance error $\breve{\boldsymbol{P}}_k$

$$\breve{\boldsymbol{P}}_k = \sum_{i=1}^{2N} \boldsymbol{w}_i^c \left(\overline{\boldsymbol{X}}_k^{(i)} \breve{\boldsymbol{X}}_k^{(i)} + \breve{\boldsymbol{X}}_k^{(i)} \overline{\boldsymbol{X}}_k^{(i)^T} + \breve{\boldsymbol{X}}_k^{(i)} \breve{\boldsymbol{X}}_k^{(i)^T} \right) \tag{5-9}$$

Substituting eq.(5-7) into eq.(3-15) yields

$$\overline{\boldsymbol{P}}_k = \sum_{i=1}^{2N} w_i^c \left(\overline{\boldsymbol{X}}_k^{(i)} \overline{\boldsymbol{X}}_k^{(i)^T} \right) + \boldsymbol{Q}_k \tag{5-10}$$

With eq.(5-9) and eq.(5-10), the predicted state covariance in the presence of model error $f_e(\cdot)$ in eq.(5-8) can be written as

$$\sum_{i=1}^{2N} w_i^c \left(\overline{\boldsymbol{X}}_k^{(i)} \overline{\boldsymbol{X}}_k^{(i)^T} \right) + \boldsymbol{Q}_k + \sum_{i=1}^{2N} w_i^c \left(\overline{\boldsymbol{X}}_k^{(i)} \breve{\boldsymbol{X}}_k^{(i)} + \breve{\boldsymbol{X}}_k^{(i)} \overline{\boldsymbol{X}}_k^{(i)^T} + \breve{\boldsymbol{X}}_k^{(i)} \breve{X}_k^{(i)^T} \right) \tag{5-11}$$

$$= \overline{\boldsymbol{P}}_k + \breve{\boldsymbol{P}}_k$$

It can be seen from eq.(5-11) that model error $f_e(\cdot)$ causes predicted state covariance's error $\breve{\boldsymbol{P}}_k$, leading to the inaccurate Kalman gain. Therefore, the state estimate will be degraded when the contact model involves error.

5.3. Random weighting unscented Kalman filter for soft tissue characterization

This chapter presents a new method to address the UKF problem of performance degradation in the presence of model error for soft tissue characterization. This method corrects the predicted state covariance in the UKF procedure using the ST concept to improve the estimation accuracy in the presence of system model error, where the random weighting estimation is constructed for the innovation covariance.

5.3.1. Correction of predicted state covariance

As analysed above, the predicted state covariance has the deviation $\breve{\boldsymbol{P}}_k$ due to system model error $f_e(\cdot)$. Using the deviation to correct the state covariance described by eq.(3-15) yields

$$\overline{\boldsymbol{P}}_k^*= \sum_{i=1}^{2N} w_i^c\left(\overline{\boldsymbol{x}}_k^{(i)} - \overline{\boldsymbol{x}}_k\ \right)\left(\overline{\boldsymbol{x}}_k^{(i)} - \overline{\boldsymbol{x}}_k\ \right)^T + \boldsymbol{Q}_k + \breve{\boldsymbol{P}}_k \tag{5-12}$$

where $\overline{\boldsymbol{P}}_k^*$ denotes the corrected predicted state covariance.

Equation (5-12) can be further written as

$$\begin{aligned}\overline{\boldsymbol{P}}_k^* &= \boldsymbol{\gamma}_k\left(\sum_{i=1}^{2N} w_i^c\left(\overline{\boldsymbol{x}}_k^{(i)} - \overline{\boldsymbol{x}}_k\ \right)\left(\overline{\boldsymbol{x}}_k^{(i)} - \overline{\boldsymbol{x}}_k\ \right)^T + \boldsymbol{Q}_k\right) \\ &= \boldsymbol{\gamma}_k\overline{\boldsymbol{P}}_k\end{aligned} \tag{5-13}$$

where $\boldsymbol{\gamma}_k$ is called the scaling factor, which is defined as

$$\boldsymbol{\gamma}_k = 1 + \frac{\breve{\boldsymbol{P}}_k}{\sum_{i=1}^{2N} w_i^c \left(\bar{\boldsymbol{x}}_k^{(i)} - \bar{\boldsymbol{x}}_k\right)\left(\bar{\boldsymbol{x}}_k^{(i)} - \bar{\boldsymbol{x}}_k\right)^T + \boldsymbol{Q}_k} \tag{5-14}$$

If we know the deviation $\breve{\boldsymbol{P}}_k$ in eq.(5-14), we can calculate the modified predicted state covariance $\bar{\boldsymbol{P}}_k^*$ directly. However, the deviation $\breve{\boldsymbol{P}}_k$ is calculated from the state prediction error $\breve{\boldsymbol{x}}_k$, which is the difference between the true state $\boldsymbol{x}_k$ and predicted state $\bar{\boldsymbol{x}}_k$. Since the true state $\boldsymbol{x}_k$ is generally unknown, it is difficult to calculate the deviation $\breve{\boldsymbol{P}}_k$ directly. Alternatively, in this chapter, the predicted state covariance is modified using the orthogonality principle.

Theorem 1 Under the orthogonality principle [64], γ_k can be determined as

$$\boldsymbol{\gamma}_k = \frac{tr\left(\sum_{j=1}^{m} \boldsymbol{v}_j \boldsymbol{Z}_{k-j}^I \boldsymbol{Z}_{k-j}^{I\,T}\right) - tr(\boldsymbol{R}_k)}{tr\left(\boldsymbol{H}_k \bar{\boldsymbol{P}}_k \boldsymbol{H}_k^T\right)} \tag{5-15}$$

where $\boldsymbol{H}_k = \left.\frac{\partial h(x)}{\partial x}\right|_{\boldsymbol{x}=\bar{\boldsymbol{x}}_k}$ and where $tr\,(\cdot)$ denotes the trace of a matrix.

Proof Consider the following analytical conditions

$$\boldsymbol{B}_{j,k} = E\left[\boldsymbol{Z}_k^{I\,T} \cdot \boldsymbol{Z}_{k+j}^I\right] = 0\,, \quad j = 1,2,\cdots \tag{5-16}$$

where $\boldsymbol{Z}_k^I = \boldsymbol{y}_k - \bar{\boldsymbol{y}}_k$ denotes the innovation vector. The eq.(5-16) is the principle of innovation orthogonality, which is used for extraction of all useful information in the innovation sequence.

Define the estimation error as

$$\hat{\boldsymbol{e}}_k = \boldsymbol{x}_k - \hat{\boldsymbol{x}}_k \tag{5-17}$$

Define the prediction error as

$$\bar{\boldsymbol{e}}_k = \boldsymbol{x}_k - \bar{\boldsymbol{x}}_k \tag{5-18}$$

Substituting eq.(3-9) and eq.(3-14) into eq.(5-18) and expanding $f(\cdot)$ by a Tailor series about $\hat{\boldsymbol{x}}_{k-1}$, the prediction error becomes

$$\bar{\boldsymbol{e}}_k = \boldsymbol{F}_k \, \hat{\boldsymbol{e}}_{k-1} + \boldsymbol{q}_k \tag{5-19}$$

where $\boldsymbol{F}_k = \left.\frac{\partial f(x)}{\partial \boldsymbol{x}}\right|_{\boldsymbol{x}=\hat{\boldsymbol{x}}_{k-1}}$

By considering modelling error $f_e(\cdot)$, eq.(5-19) become

$$\bar{\boldsymbol{e}}_k = (\boldsymbol{F}_k + \boldsymbol{F}_k^e) \, \hat{\boldsymbol{e}}_{k-1} + \boldsymbol{q}_k \tag{5-20}$$

where $\boldsymbol{F}_k^e = \left.\frac{\partial \, f_e(x)}{\partial x}\right|_{\boldsymbol{x}=\hat{\boldsymbol{x}}_{k-1}}$

Assuming the measurement model is accurate. Similar to eq.(5-19), the innovation vector $\boldsymbol{Z}_k^I$ can be defined as

$$\boldsymbol{Z}_k^I = \boldsymbol{H}_k \, \bar{\boldsymbol{e}}_k + \boldsymbol{r}_k \tag{5-21}$$

where $\boldsymbol{H}_k = \left.\frac{\partial h(x)}{\partial x}\right|_{\boldsymbol{x}=\hat{\boldsymbol{x}}_{k-1}}$

$\bar{\boldsymbol{P}}_k$ is defined by

$$\bar{\boldsymbol{P}}_k = E\,[(\boldsymbol{x}_k - \bar{\boldsymbol{x}}_k)(\boldsymbol{x}_k - \bar{\boldsymbol{x}}_k)^T] \tag{5-22}$$

$\boldsymbol{P}_{\bar{\boldsymbol{x}}_k \bar{\boldsymbol{y}}_k}$ is defined by

$$\boldsymbol{P}_{\bar{x}_k\bar{y}_k} = E\left[(\boldsymbol{x}_k - \bar{\boldsymbol{x}}_k)(\boldsymbol{y}_k - \bar{\boldsymbol{y}}_k)^T\right] \tag{5-23}$$

Substituting eq.(5-21) into eq.(5-22) with eq.(5-17) yields

$$\begin{aligned}\boldsymbol{P}_{\bar{x}_k\bar{y}_k} &= E\left[(\boldsymbol{x}_k - \bar{\boldsymbol{x}}_k)(\boldsymbol{H}_k(\boldsymbol{x}_k - \bar{\boldsymbol{x}}_k) + \boldsymbol{r}_k)^T\right] \\ &= E\left[(\boldsymbol{x}_k - \bar{\boldsymbol{x}}_k)(\boldsymbol{x}_k - \bar{\boldsymbol{x}}_k)^T\boldsymbol{H}_k{}^T + \boldsymbol{r}_k{}^T\right] \\ &= \bar{\boldsymbol{P}}_k\boldsymbol{H}_k{}^T\end{aligned} \tag{5-24}$$

Substituting eq.(5-20) into eq.(5-21) yields

$$\boldsymbol{Z}_k^I = \boldsymbol{H}_k[(\boldsymbol{F}_k + \boldsymbol{F}_k^e)\hat{\boldsymbol{e}}_{k-1} + \boldsymbol{q}_k] + \boldsymbol{r}_k \tag{5-25}$$

Substituting eq.(5-25) into eq.(5-16) leads to

$$\begin{aligned}\boldsymbol{B}_{j,k} &= E\left\{\left[\boldsymbol{H}_{k+j}\left((\boldsymbol{F}_{k+j} + \boldsymbol{F}_{k+j}^e)\hat{\boldsymbol{e}}_{k+j-1} + \boldsymbol{q}_{k+j}\right) + \boldsymbol{r}_{k+j}\right] \times \left[\boldsymbol{H}_k\left((\boldsymbol{F}_k + \boldsymbol{F}_k^e)\hat{\boldsymbol{e}}_{k-1} + \boldsymbol{q}_k\right) + \boldsymbol{r}_k\right]^T\right\} \\ &= E\left\{\left[\boldsymbol{H}_{k+j}(\boldsymbol{F}_{k+j} + \boldsymbol{F}_{k+j}^e)\left(\boldsymbol{x}_{k+j-1} - \bar{\boldsymbol{x}}_{k+j-1} - K_{k+j-1}(\boldsymbol{y}_{k+j-1} - \bar{\boldsymbol{y}}_{k+j-1})\right)\right]\right. \\ &\qquad \left.\times \left[\boldsymbol{H}_k\left((\boldsymbol{F}_k + \boldsymbol{F}_k^e)\hat{\boldsymbol{e}}_{k-1} + \boldsymbol{q}_k\right) + \boldsymbol{r}_k\right]^T\right\} \\ &= E\left\{\left[\boldsymbol{H}_{k+j}(\boldsymbol{F}_{k+j} + \boldsymbol{F}_{k+j}^e)\left((\boldsymbol{F}_{k+j-1} + \boldsymbol{F}_{k+j-1}^e)\,\hat{\boldsymbol{e}}_{k+j-2} - \boldsymbol{K}_{k+j-1}(\boldsymbol{H}_k[(\boldsymbol{F}_k + \boldsymbol{F}_k^e)\hat{\boldsymbol{e}}_{k+j-2}])\right)\right]\right. \\ &\qquad \left.\times \left[\boldsymbol{H}_k\left((\boldsymbol{F}_k + \boldsymbol{F}_k^e)\hat{\boldsymbol{e}}_{k-1} + \boldsymbol{q}_k\right) + \boldsymbol{r}_k\right]^T\right\} \\ &= E\left\{\left[\boldsymbol{H}_{k+j}(\boldsymbol{F}_{k+j} + \boldsymbol{F}_{k+j}^e)(I - \boldsymbol{K}_{k+j-1}\boldsymbol{H}_k(\boldsymbol{F}_k + \boldsymbol{F}_k^e)\hat{\boldsymbol{e}}_{k+j-2})\right]\right. \\ &\qquad \left.\times \left[\boldsymbol{H}_k\left((\boldsymbol{F}_k + \boldsymbol{F}_k^e)\hat{\boldsymbol{e}}_{k-1} + \boldsymbol{q}_k\right) + \boldsymbol{r}_k\right]^T\right\} \\ &= \boldsymbol{H}_{k+j}(\boldsymbol{F}_{k+j} + \boldsymbol{F}_{k+j}^e) \times \left(\prod_{i=k+1}^{k+j-1}(I - \boldsymbol{K}_i\boldsymbol{H}_i)(\boldsymbol{F}_i + \boldsymbol{F}_i^e)\right) \times (\bar{\boldsymbol{P}}_{\bar{x}_k\bar{y}_k} - \boldsymbol{K}_k\boldsymbol{B}_{0,k})\end{aligned} \tag{5-26}$$

where the system and measurement noise covariances are Gaussian white noises, i.e., $E(\boldsymbol{r}_i\boldsymbol{r}_j{}^T) = 0, E(\boldsymbol{q}_i\boldsymbol{q}_j{}^T) = 0\ E(\boldsymbol{q}_i\boldsymbol{r}_j{}^T) = 0\ (i \neq j)$.

$\boldsymbol{B}_{0,k}$ is the innovation covariance and its arithmetic mean estimation can be represented as

$$\boldsymbol{B}_{0,k} = \frac{1}{m}\sum_{j=1}^{m} \boldsymbol{Z}_{k-j}^{I} \boldsymbol{Z}_{k-j}^{I\,T} \tag{5-27}$$

where m is the window width, which is the number of measurements within the window $(t_{k-1}, t_{k-2}, \ldots, t_{k-m})$.

Applying the random weighting concept to eq.(5-27), the random weighting estimation of $\boldsymbol{B}_{0,k}$ can be written as

$$\boldsymbol{B}_{0,k} = \sum_{j=1}^{m} \boldsymbol{v}_j \, \boldsymbol{Z}_{k-j}^{I} \boldsymbol{Z}_{k-j}^{I\,T} \tag{5-28}$$

where $\boldsymbol{v}_j$ is the random weighting factor which meets the condition $\sum_{j=1}^{m} \boldsymbol{v}_j = 1$.

To meet condition of eq.(5-16), eq.(5-26) is required to be zero which leads to the condition

$$\overline{\boldsymbol{P}}_{\bar{x}_k \bar{y}_k} - \boldsymbol{K}_k \boldsymbol{B}_{0,k} = 0 \tag{5-29}$$

By Taylor series, the predicted measurement covariance given by eq.(3-17) can be further written as

$$\boldsymbol{P}_{\bar{y}_k} = \sum_{i=1}^{2N} w_i^c \left(\bar{\boldsymbol{y}}_k^{(i)} - \bar{\boldsymbol{y}}_k\right)\left(\bar{\boldsymbol{y}}_k^{(i)} - \bar{\boldsymbol{y}}_k\right)^T + \boldsymbol{R}_k \tag{5-30}$$

$$= \boldsymbol{H}_k \boldsymbol{P}_{\boldsymbol{x}} \boldsymbol{H}_k^{\,T} + \boldsymbol{R}_k$$

where $\boldsymbol{H}_k = \left.\frac{\partial h(\boldsymbol{x})}{\partial \boldsymbol{x}}\right|_{\boldsymbol{x}=\hat{\boldsymbol{x}}_{k-1}}$.

Replacing $\overline{\boldsymbol{P}}_k$ in eq.(5-30) with the corrected predicted state covariance $\overline{\boldsymbol{P}}_k^*$ in eq.(5-13) yields

$$\boldsymbol{P}_{\bar{y}_k}^* = \left[\boldsymbol{H}_k \boldsymbol{\gamma}_k \overline{\boldsymbol{P}}_k \boldsymbol{H}_k^T\right] + \boldsymbol{R}_k \tag{5-31}$$

$$= \boldsymbol{\gamma}_k \left[\boldsymbol{H}_k \overline{\boldsymbol{P}}_k \boldsymbol{H}_k^{\,T}\right] + \boldsymbol{R}_k$$

where $\boldsymbol{P}_{\bar{y}_k}^{*}$ denotes the modified predicted measurement covariance.

Similarly, eq.(5-24) can be further written as

$$\overline{\boldsymbol{P}}_{\bar{x}_k\bar{y}_k} = \boldsymbol{\gamma}_k \boldsymbol{P}_k {\boldsymbol{H}_k}^T \tag{5-32}$$

Substituting eq.(5-31) and eq.(5-32) into eq.(5-29) and further holding it, we have

$$\boldsymbol{\gamma}_k \left[\boldsymbol{H}_k \boldsymbol{P}_k {\boldsymbol{H}_k}^T\right] = \boldsymbol{Y}_{0,k} - \boldsymbol{R}_k \tag{5-33}$$

Subtitling eq.(5-28) into eq.(5-33) yields

$$\boldsymbol{\gamma}_k \left[\boldsymbol{H}_k \boldsymbol{P}_k {\boldsymbol{H}_k}^T\right] = \sum_{j=1}^{m} \boldsymbol{v}_j \left[\boldsymbol{Z}_{k-j}^{l} {\boldsymbol{Z}_{k-j}^{l}}^T\right] - \boldsymbol{R}_k \tag{5-34}$$

From eq.(5-34), $\boldsymbol{\gamma}_k$ is determined as

$$\boldsymbol{\gamma}_k = \frac{tr\left(\sum_{j=1}^{m} \boldsymbol{v}_j \boldsymbol{Z}_{k-j}^{l} {\boldsymbol{Z}_{k-j}^{l}}^T\right) - tr(\boldsymbol{R}_k)}{tr\left(\boldsymbol{H}_k \overline{\boldsymbol{P}}_k {\boldsymbol{H}_k}^T\right)} \tag{5-35}$$

where $tr(\cdot)$ denotes the trace of a matrix.

The proof of **Theorem 1** is completed.

Substituting (5-35) into (5-13), the corrected predicted state covariance is calculated as

$$\overline{\boldsymbol{P}}_k^{*} = \left(\frac{tr\left(\sum_{j=1}^{m} \boldsymbol{v}_j \boldsymbol{Z}_{k-j}^{l} {\boldsymbol{Z}_{k-j}^{l}}^T\right) - tr(\boldsymbol{R}_k)}{tr\left(\boldsymbol{H}_k \overline{\boldsymbol{P}}_k {\boldsymbol{H}_k}^T\right)}\right) \overline{\boldsymbol{P}}_k \tag{5-36}$$

From the above, we can see that the proposed RWSTUKF takes into account system model error by correcting the predicted state covariance. Further, the determination process of the scaling factor $\boldsymbol{\gamma}_k$ does not involve the calculation of Jacobian matrix.

5.3.2. Random weighting UKF algorithm

The detailed procedure of the proposed method is described in Figure 5-1. In the absence of system model error, the proposed method just follows the standard UKF procedure. In the presence of system model error, the predicted state covariance is corrected to compensate system model error and further re-estimate the system state. It can be seen from Figure 5-1, the proposed method only repeats the process of measurement update step in the Kalman filter procedure, which is explained in Chapter 3, to maintain the computational efficiency.

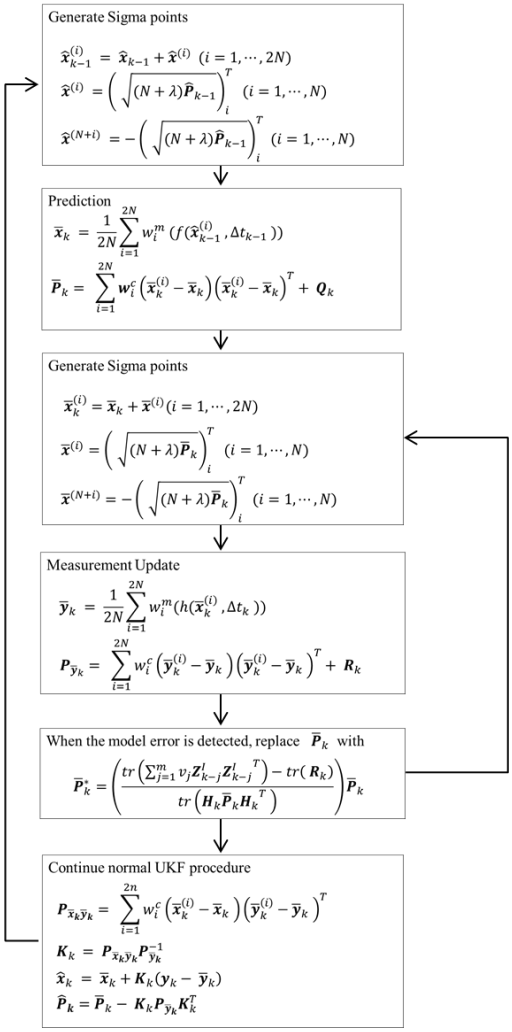

Figure 5-1 Architecture of RWSTUKF

5.4. Performance evaluation and discussion

Simulations were conducted to comprehensively evaluate the proposed RWSTUKF. The simulation trials were conducted to evaluate the performance of RWSTUKF under the three different model errors (i.e., initial state estimation error, model simplification error, and local modelling error). The interaction force signals were generated based on the nonlinear H-C contact model. Based on the estimated parameters of the nonlinear H-C model, the interaction forces were reconstructed and compared with the interaction force. Comparison analysis of RWSTUKF with UKF was also discussed.

5.4.1. Initial state estimation error

The following parameters of the nonlinear H-C contact model are constant,

$$K_0 = 150\,, B_0 = 2\,, n_0 = 1\; p_0, = 1 \tag{5-37}$$

Above parameters were used to generate interaction forces when the displacement is increased continuously. In order to simulate the initial state error, the initial values of the H-C model parameters were selected as

$$K_k = 10\,, B_k = 1\,, n_k = 2\,, p_k = 1.05 \tag{5-38}$$

Comparing eq.(5-37) and eq.(5-38), it can be easily seen that the initial value of state estimation involves a large error.

Trials were conducted by both UKF and RWSTUKF to analyse the effect of the initial state estimation error. The velocity was set to $\dot{d}(t_k)$=0.1mm, and the window size m = 4. $\boldsymbol{Q}_k$ was set $diag\ (0.01mN)_{7\times7}$ and $\boldsymbol{R}_k$ was set $diag\ (0.01mN)_{2\times2}$ and $\theta_T = 0.007$.

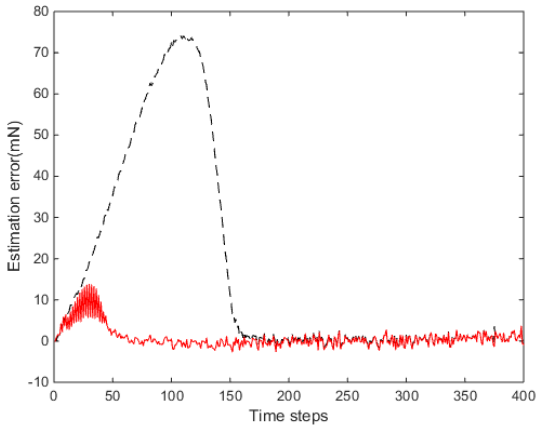

Figure 5-2 Estimation errors by both of UKF and RWSTUKF when the inaccurate initial condition: The black dash line is the estimation error from the conventional UKF while the red solid line shows the estimation error from RWSTUKF

Figure 5-2 shows the estimation errors of both UKF and RWSTUKF under the initial state estimation error. Due to the influence of the initial error, the estimation error by UKF is rapidly increased and converged after 150-time steps, leading to the maximum estimation error of 73.265mN. However, the estimation error by RWSTUKF is converged after 50-time steps. This means the convergence speed of RWSTUKF is three times faster than that of UKF. The resultant maximum estimation error of RWSTUKF is 13.887mN, which is about six times smaller than that of UKF. This is because RWSTUKF can dynamically adjust the predicted state covariance to restrain the disturbance of the initial error on the filtering solution, leading to the improved accuracy than UKF. Table 5-1 summarises the estimation errors

from both UKF and RWSTUKF. The RMSE is 2.9133mN for RWSTUKF, whereas 30.2395mN for UKF.

Table 5-1 Estimation errors of UKF and RWSTUKF in the presence of initial state error

Errors (mN)	UKF	RWSTUKF
Mean error	16.8818	1.8092
Max error	74.2650	13.887
RMSE	30.2395	2.9133

5.4.2. Model simplification error

The system model error from the simplification of the system state model was considered. Note that the nonlinearity of the H-C model is increased by considering *p* as a constant value as studied in Chapter 3. In order to reduce the complexity of nonlinearity, the state model in eq.(3-1) is simplified as eq.(5-39) by setting parameter *p* = 1 as

$$F = Kd^n + Bd^n\dot{d} \tag{5-39}$$

The interaction force signal was still generated according to eq.(3-1) under the same conditions as the earlier simulation except that the initial condition is selected as

$$K_0 = 10\,, B_0 = 1\,, n_0 = 2\,, p_0 = 1.05 \tag{5-40}$$

Trials were conducted by both UKF and RWSTUKF. The velocity was $\dot{d}(t)_k$=0.01, and the window size *m* = 4. $\boldsymbol{Q}_k$ was set $diag(0.1mN)_{7\times7}$ and $\boldsymbol{R}_k$ was set $diag(0.1mN)_{2\times2}$.

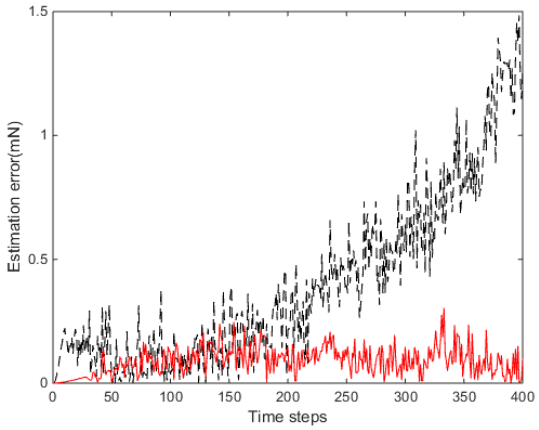

Figure 5-3 Estimation errors by both of UKF and RWSTUKF in the presence of system model error: The black dash line is the estimation error from the conventional UKF while the red solid line shows the estimation error from RWSTUKF

Figure 5-3 is the estimation errors by both UKF and RWSTUKF under the error of model simplification. The estimation error of UKF is bounded with the maximum error of 0.4582mN within 200-time steps. Note that although the error boundary would be different according to the application, the boundary could be calculated through a large volume of empirical test data. However, after 200-time steps, due to the disturbance by the error of model simplification, the estimation error of UKF is drastically increased, leading to the maximum error of 1.4844mN at the end of the simulation. In contrast, within 40-time steps, the estimation error of RWSTUKF is very small, leading to the maximum estimation error of 0.0444mN. After 40-time steps, in spite of the relatively large increase, the estimation error of RWSTUKF is bounded with the maximum error of 0.3039mN, which is even smaller than that of UKF within 200-time steps. The estimation results demonstrate that the RWSTUKF was able to compensate system model error by dynamically modifying the predicted state covariance. Table 5-2 shows the estimation errors by both UKF and RWSTUKF. The RMSE

and mean error are 0.5394mN and 0.4068mN for UKF, while they are 0.1063mN and 0.08977mN for RWSTUKF. Thus, it is clear that RWSTUKF outperforms UKF.

Table 5-2 Estimation errors of UKF and RWSTUKF with simplified system model

Errors (mN)	UKF	RWSTUKF
Mean error	0.4068	0.0897
Max error	1.4844	0.3039
RMSE	0.5394	0.1063

5.4.3. Local modelling error

The local modelling error could happen due to many instant uncertain external or internal effects during RAMIS. For example, in a needle insertion procedure, when needle encounters unexpected materials such as tumour or small bone, the UKF-based estimator instantly has estimation error. This is because the system model could not account the dynamic variation of the contact environment. The simulation was designed to evaluate the performance of the proposed method under this local modelling error condition. A constant prediction error of [0 0 0 0.8 0.8 0 0 0] was added to the predicted state described by (3-14) for the period between time point 200 and 220. $\boldsymbol{Q}_k$ was set $diag(0.01mN)_{7\times7}$ and $\boldsymbol{R}_k$ was set $diag(0.01mN)_{2\times2}$. The other parameters are the same as the simulation case in Section 5.4.1.

Figure 5-4 represents the estimation errors by both UKF and RWSTUKF with the local modelling error. It is clear that the estimation error of UKF is increased dramatically during the time period (200 ~ 220-time steps) with the added constant error, leading to the maximum estimation error of 6.7853mN. In contrast, the estimation error curve of the proposed RWSTUKF does not involve a notable change during the entire simulation time, especially for the time period with the added constant error. This is because the predicted state covariance was corrected to account for the added error during the time period (200 ~ 220-time steps). As shown in Table 5-3 represents the estimation errors by both UKF and RWSTUKF with the local modelling error. It is clear that the estimation error of UKF is increased dramatically during the time period (200 ~ 220-time steps) with the added constant error, leading to the maximum estimation error of 6.7853mN. In contrast, the estimation error curve of the proposed RWSTUKF does not involve a meaningful change during the entire simulation time, especially for the time period with the added constant error. This is because the predicted state covariance was corrected to account for the added error during the time period (200 ~ 220-time steps).

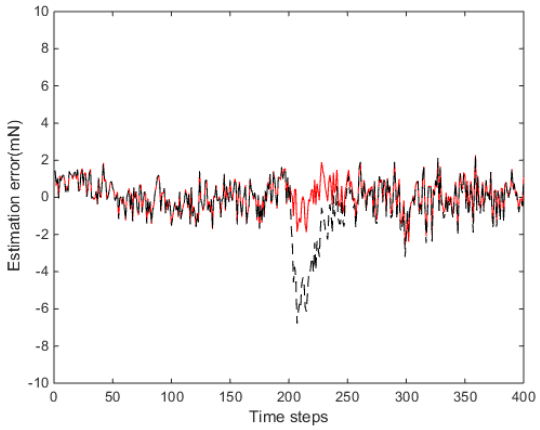

Figure 5-4 Estimation errors by both of UKF and RWSTUKF with constant prediction error in time points 200-220: The black dash line is the estimation error from the conventional UKF while the red solid line shows the estimation error from RWSTUKF

Table 5-3 Estimation errors of UKF and RWSTUKF with constant modelling error

Errors (mN)	**UKF**	**RWSTUKF**
Mean error	0.9531	0.6911
Max error	6.7853	2.5880
RMSE	1.4200	0.8590

5.4.4. Experiments and analysis

The two experimental cases, described in Section 4.3, were also considered for the performance evaluation of RWSTUKF. The first case was the robotic needle insertion based on the experimental data in the literature [55] and the second one was the DMA

indentation test on the phantom tissue. The experimental setup and associated parameters were the same as those in Section 4.3.

Figure 5-5 (a) shows the reconstructed force for the case of robotic needle insertion using the data in the literature [55] described in Section 4.3.2.1. As discussed in Section 4.3.2.1, a large estimation error occurs at the four cusps at the displacements of around 20mm, 29mm, 32mm, and 36mm since the employed H-C model does not explicitly describe the cusps in the force signal. However, Figure 5-5 (a) has clearly shown that the reconstructed force by RWSTUKF is extremely close to the interaction force data (reference value), especially at those four cusps. The resultant mean error is 0.0044N, which is significantly smaller than that of RAUKF (0.020N).

Figure 5-5 (b) shows the reconstructed force by RWSTUKF for the DMA indentation case described in Section 4.3.2.2. As discussed in Section 4.3.2.2, estimation errors were caused by the three abrupt changes in the force curve at around 0.9s, 1.8s and 2.7s, which represent sudden changes in RAMIS. However, Figure 5-5 (b) has shown clearly that the reconstructed force by RWSTUKF is extremely close to the interaction force data (reference value). The average estimation error of RWSTUKF is only 0.0014N, which is much smaller than that of RAUKF (0.0062N).

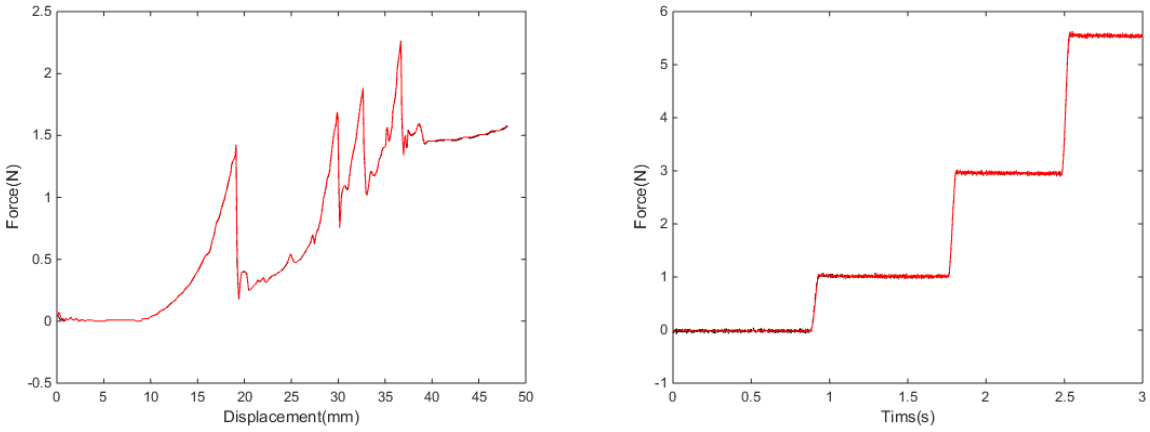

(a) Literature Data (b) DMA indentation

Figure 5-5 Reconstructed forces by RWSTUKF (a) with data from literature [55], (b) with experiment data from DMA test: The black dash line is the interaction force signal (reference value) while the red solid line shows the reconstructed forces by RWSTUKF

Table 5-4 lists the detailed estimation errors of RWSTUKF for both cases. For the case of robotic needle insertion, the RMSE and maximum error of RWSTUKF are 0.0084N and 0.1275N, which are much smaller than those of RAUKF (RMSE: 0.039N; and maximum error: 0.205N). The case of DMA indentation also demonstrates that RWSTUKF (RMSE: 0.0018N; and maximum error: 0.0113N) outperforms RAUKF (RMSE: 0.0098N; and maximum error: 0.0638N).

Table 5-4 Estimation errors of RWSTUKF

Error (N)	**Needle insertion**	**DMA indentation**
Mean Error	0.0044	0.0014
Maximum Error	0.1275	0.0113
RMSE	0.0084	0.0018

5.5. Summary

This chapter presents RWSTUKF for nonlinear soft tissue characterization in the presence of system model error. RWSTUKF incorporated a dynamic scaling factor in the predicted state covariance to online compensate the model errors. This scaling factor was determined by combining the principle of innovation orthogonality with the random weighting concept to avoid cumbersome computation of Jacobian matrix and improve the approximation accuracy of the actual innovation. The proposed RWSTUKF not only outperforms UKF in the presence of the system model error, but it also maintains the computational efficiency by correcting the predicted state covariance only in the time segments with system model error. Simulation and experimental results demonstrated that the proposed RWSTUKF is strongly robust against the system model error for online soft tissue characterization.

6. Master-slave robotic system for soft tissue characterization

6.1. Introduction

A new, online soft tissue characterization method with a combination of the UKF and the H-C model was introduced in Chapter 3. This method was further improved, resulting in RAUKF in Chapter 4, to deal with unknown noise statistics. A second improvement RWSTUKF in Chapter 5 deals with system model error. The experiments using DMA and simulations were conducted to verify the proposed methods.

Based on the earlier chapters, this chapter presents a bilateral master-slave robotic system for soft tissue characterization, where the proposed methods have been implemented respectively as a nonlinear state observer for comparison analysis. A rupture detection approach was further established based on RWSTUKF and integrated into the master-slave robotic system to detect rupture events that occurred in needle insertion. Experiments were conducted with the master-slave robotic system to evaluate the performances of the various nonlinear estimation methods and the rupture detection method proposed in this thesis for RAMIS.

6.2. System design

The master robot was implemented by PHANToM OMNI [65], which is a portable haptic device with six Degrees of Freedom (DOF) developed by SensAble Technologies. A 1-DOF robot (not only for needle insertion but also for robotic indentation) was designed as the slave robot to mimic the movements of the master robot to carry out robotic indentation on a phantom tissue, or needle insertion, into the porcine liver sample (see Figure 6-1). A slave robot was developed with a linear magnetic motor (LM2070_08011_FMM, FAULHABER) to generate the linear motion, a motor driver (MCLM3006, FAULHABER) to control the linear magnetic motor efficiently, the surgical tool (either an indenter of diameter 3mm or a needle of diameter 5mm) and a 6-axis force sensor (Nano 17 and FTIFPS1, ATI) to measure the interaction force between the surgical tool and tissue samples. The force sensor was attached to the end of the linear magnetic motor so that both can move together to effectively measure the interaction force. The phantom soft tissue was made up of silicone rubber, which has similar characteristics to human tissue [61]. The phantom tissue was made in a cubic shape (3cm × 8cm × 6cm). Two adjustable supports were designed to support the linear motor and the tissue sample, respectively. The displacement and velocity of the slave robot were derived from the position incremental encoder, which is attached to the linear motor.

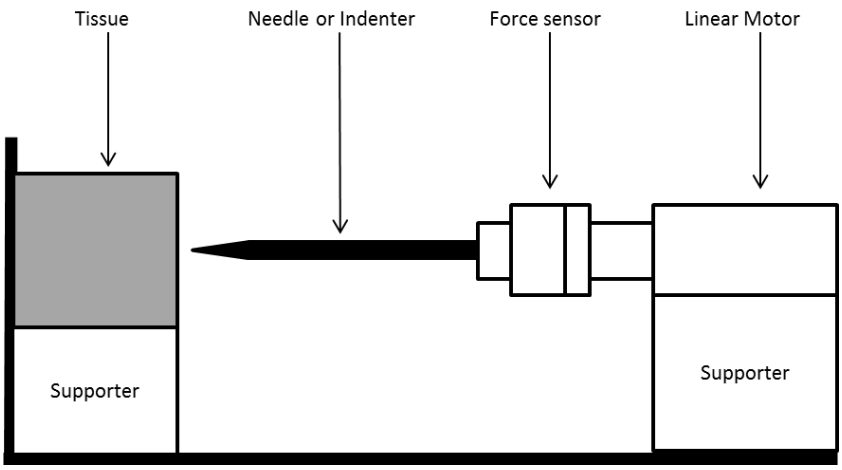

Figure 6-1 System components

A bilateral controller was developed with MATLAB to control the slave robot with the master robot. The position information of PHANToM OMNI (the master robot) was delivered every 1ms to the bilateral controller to control the slave robot. Since the slave robot is 1-DOF, only X-axis position information was used in the bilateral controller. In order to control the position of the slave robot based on the delivered position information of the master robot, the magnetic linear motor is controlled via serial communication by the built-in PID controller in the motor drive. The interaction force between the slave robot and the tissue sample was measured with the force sensor and delivered to the MATLAB control system through the USB-based DAQ board (USB-6210, NI).

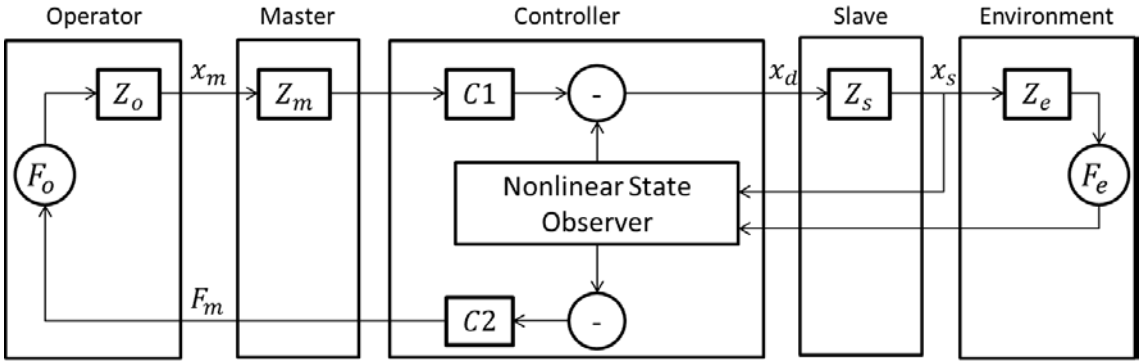

Figure 6-2 System framework

The system framework is shown in Figure 6-2, where the nonlinear state observer was used to estimate the nonlinear parameters of the H-C model to be able to monitor the contact environment in real time. x_m, x_d and x_s are the displacements for the master robot, controller and slave robot, respectively. $C1$ and $C2$ are the control gains. Z_o, Z_m, Z_s and Z_e are the impedances caused by the operator, master robot, slave robot and environment, respectively. F_o, F_e and F_m are the forces from the operator, the environment and the master robot.

6.3. Experimental analysis

For the comparison analysis, the nonlinear state observer in the master-slave robotic system was implemented by RLS, UKF, RAUKF, and RWSTUKF respectively. Experiments were designed into two categories. One focused on the robotic indentation on the phantom tissue sample, the other focused on the needle insertion into the porcine liver sample to identify the existence of a rupture event.

The user controls the 1-DOF master-slave device to carry out the robotic indentation or needle insertion test. The displacement was obtained from the built-in encoder. The interaction force between the tissue sample and the end-effector of the slave robot was measured with the force sensor. Based on the obtained force and displacement information, the nonlinear state observer estimates the nonlinear parameters of the H-C model. The interaction force was reconstructed based on the estimated H-C model parameters and the displacement information, and further compared with the measured interaction forces reference to calculate the estimation error.

6.3.1. Robotic indentation

The first category of experiments was robotic indentation test on the phantom soft tissue. The experimental setup is shown in Figure 6-3. The initial state and noise covariance was set as $\boldsymbol{x}_0$= [0.1, 0.1, 0.01, 0.0001, 0.0001, 1, 1], $\boldsymbol{Q}_k$ was set $diag\ (.01N)_{7\times7}$ and $\boldsymbol{R}_k$ was set $diag\ (0.01N)_{2\times2}$. The window size was set to m = 4.

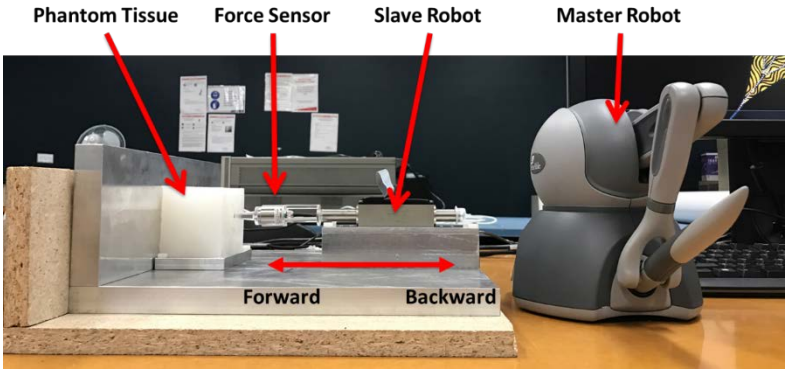

Figure 6-3 System for the indentation experiment

The interaction force is increased when the indenter moves forward to press the phantom soft tissue, but decreased when the indenter is controlled to move backward. The interaction force becomes zero when there is no contact between the indenter and phantom tissue. The measured interaction force is indicated by the black dash line in Figure 6-4.

The reconstructed forces by RLS, UKF and RAUKF are shown in Figure 6-4. It is clear that the reconstructed force by UKF follows the dynamic variations of the interaction force, while the one by RLS does not. The mean estimation error of UKF (0.3015N) is more than five times smaller than that of RLS (1.6432N). The RMSE of UKF is 0.6319N, while that of RLS is 2.0899N. Despite a better agreement with the reference value (interaction force) than RLS, UKF involves a large estimation error, with the maximum error of 5.6628N at around 36s. This is because the constant noise covariance does not represent the system correctly, especially after 33s when the interaction force starts to change abruptly. RAUKF improves the estimation accuracy of UKF at 36s, leading to the mean error of 0.1532N and RMSE of 0.2666N, which are more than two times smaller than those of UKF and ten times smaller than those of RLS. The maximum error of RAUKF is only 1.8511N.

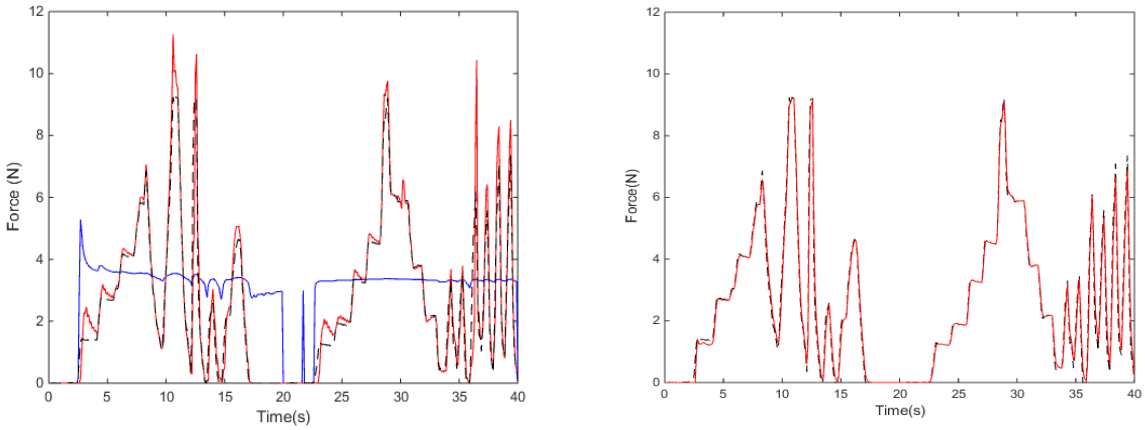

(a) UKF and RLS (b) RAUKF

Figure 6-4 Reconstructed forces by RLS, UKF and RAUKF for the case of robotic indentation: The black dash lines indicate the interaction force (the reference), the red solid lines in (a) and (b) the reconstructed forces by UKF and RAUKF, and the blue solid line in (a) the reconstructed force by RLS

Figure 6-5 represents the reconstructed force by RWSTUKF. It can be seen that RWSTUKF has higher estimation accuracy than RAUKF. Its mean error and RMSE are 0.1052N 0.2017N. In particular, when the interaction force changes dramatically such as at 8s and after 35s, the reconstructed force by RWSTUKF is extremely close to the interaction force than that of RAUKF. The detailed estimation error analysis is shown in Table 6-1.

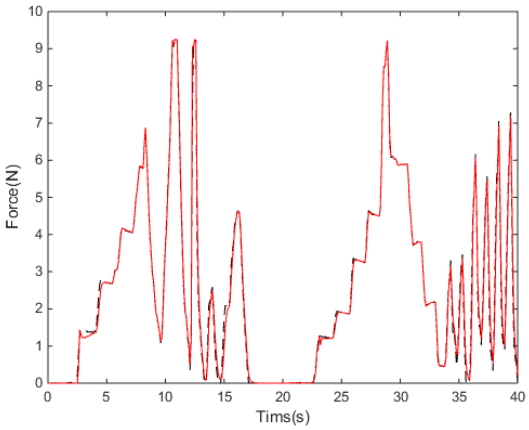

Figure 6-5 Reconstructed force by RWSTUKF for the case of robotic indentation: The black dash line indicates the interaction force, and the red solid line the reconstructed force

Table 6-1 Estimation errors of indentation experiment

Errors (N)	RLS	UKF	RAUKF	RWSTUKF
Mean error	1.6432	0.3015	0.1532	0.1052
Max error	5.8360	5.6628	1.8511	1.6282
RMSE	2.0899	0.6319	0.2666	0.2017

6.3.2. Robotic needle insertion

The second experiment was the needle insertion test with the porcine liver sample. Instead of the indenter in the robotic indentation case, a needle of diameter 3mm is used to pierce the porcine liver sample. This category of experiments was conducted under the similar conditions as the case of robotic indentation in Section 6.3.1. The user manipulated the master robot to move the needle forward to press and further penetrate the porcine liver sample. Subsequently, the needle was moved backward and extracted from the tissue

sample. The size of window m was 5, $\boldsymbol{x}_0$ = [0.1, 0.1, 0.01, 0.0001, 0.0001, 1 1], $\boldsymbol{Q}_k$ was set $diag\ (0.0001mN)_{7\times7}$ and $\boldsymbol{R}_k$ was set $diag\ (0.01mN)_{2\times2}$.

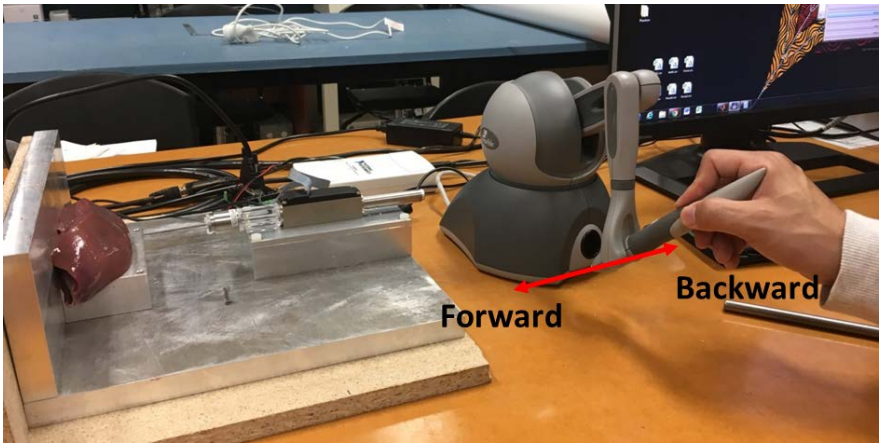

Figure 6-6 Experiment setup for robotic needle insertion into porcine liver

Figure 6-7 shows the estimation results from the case of robotic needle insertion. Before the contact of the needle with the porcine liver sample, the interaction force was zero. Once the needle was in contact with the porcine liver sample, the interaction force started to increase rapidly. The maximum interaction force of 2.3556N was reached when the needle was penetrating into the liver sample. After the penetration into the liver sample, the interaction force dropped drastically in a brief period of time. It is shown clearly that the interaction force decreases dramatically once the needle is moved backward at around 6s to extract from the tissue sample. The interaction force becomes zero again after the needle was completely extracted from the porcine liver sample.

Figure 6-7 (a) shows the reconstructed forces by RLS and UKF, while Figure 6-7 (b) shows the reconstructed force by RWSTUKF. In Figure 6-7 (a), it is noticeable that the reconstructed

force by RLS does not follow the interaction force, while that of UKF has a good agreement with the interaction force. However, it can also be seen that the reconstructed force by UKF involves a large deviation at the rupture point marked by the black dash circle in Figure 6-7 (a), with the maximum error of 0.3350N. As shown in Figure 6-7 (b), RAUKF improves the estimation accuracy of UKF at the rupture point, reducing the maximum error to 0.0830N. After the rupture point, the difference between the reconstructed forces by UKF and RAUKF becomes more distinct. The reconstructed force by UKF has a clear deviation from the interaction force, with the mean error of 0.0198N. In contrast, that of RAUKF is very close to the interaction force, with the mean error of 0.0039N.

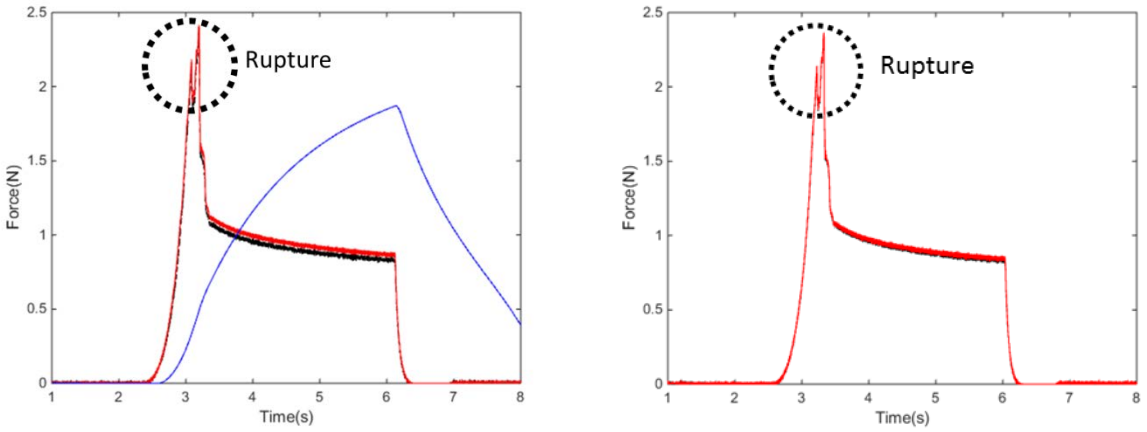

(a) UKF and RLS (b) RAUKF

Figure 6-7 Reconstructed forces by RLS, UKF and RAUKF for the case of robotic needle insertion: The black dash lines in (a) and (b) indicate the interaction force (reference), the red solid lines in (a) and (b) indicate the reconstructed forces by UKF and RAUKF, and the blue solid line in (a) indicates the reconstructed force by RLS

The above analyses show that RAUKF has a better estimation performance than UKF and RLS. The mean estimation error of UKF is 0.0198N and that of RLS is 0.5894N, whereas that

of RAUKF is much smaller, which is only 0.039N. The RMSE of RAUKF is 0.0057N, which is also much smaller than that of UKF (0.0208N) and that of RLS (0.7679N). The detailed estimation errors are shown in Table 6-2.

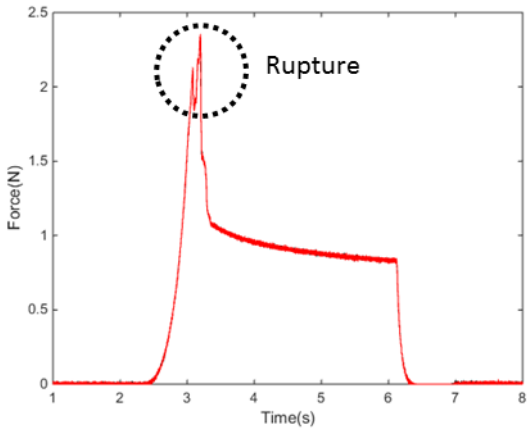

Figure 6-8 Reconstructed force by RWSTUKF for the case of robotic needle insertion: The black dash line and red solid line indicate the interaction force (reference) and reconstructed force

Figure 6-8 shows the reconstructed force by RWSTUKF. The resultant mean error and RMSE are 0.012N and 0.047N, which are much smaller than those of RLS, UKF and RAUKF. The maximum error of RWSTUKF also occurs at the rupture point which is marked by the black dash circles in Figure 6-8. It is 0.0131N, which is also smaller than that of RAUKF (0.0830N). After the rupture point, RWSTUKF is extremely close to the interaction curve. The rigorous comparison analysis of the estimation performance at rupture event is considered in the following session.

Table 6-2 Estimation errors of needle insertion into a porcine liver sample experiment

Errors (N)	RLS	UKF	RAUKF	RWSTUKF
Mean error	0.5894	0.0198	0.0039	0.0012
Max error	1.8657	0.3350	0.0830	0.0131
RMSE	0.7679	0.0280	0.0057	0.0047

6.3.3. Rupture detection

During needle insertion, the perception of rupture events provides haptic clues to the surgeon [66, 67]. When a needle is in contact with soft tissue before penetrating the soft tissue, the interaction force is changed gradually. When the needle starts to penetrate the soft tissue, however, the interaction force decreases dramatically. Therefore, rupture events can be detected by monitoring the abrupt force transitions during needle insertion.

Direct filtering is a simple method to identify abrupt changes in force signal with its differential values [66]. However, this method is not effective for rupture detection since it cannot guarantee that the detected abrupt change in the force signal always corresponds to a rupture event. The differential profile of the force signal in the case of fast needle extraction is quite similar to that of rupture events. Further, measurement noise in force signal also makes it difficult for the method to detect a rupture event [66].

Barbe et al. proposed a fault detection method to improve the rupture detecting performance during needle insertion into soft tissue [66]. This was a statistical method based on a hypothesis test. Instead of using the derivative in force signal, this method

detected the rupture events with the prediction error, which is the difference between the predicted and measured forces. Since the values of the prediction error tend to get close to zero in normal condition and vary abruptly at the rupture event, the prediction error was able to be employed for rupture detection. However, in this method, the predicted force was calculated from soft tissue parameters estimated by RLS. As discussed in Chapter 3, RLS is a linear regression method, which is unsuitable for characterization of nonlinear soft tissue behaviours. Thus, the fault detection method suffers from the poor estimation accuracy of RLS, leading to the limited performance for rupture detection. Elgezua et al. developed an event classification algorithm for rupture detection [67]. However, this method requires prior knowledge of the statistics of puncture force for each type of soft tissue. Since soft tissue properties are dynamically changed as per various conditions, such as different tissue layers and different physiological conditions, it is difficult to satisfy this requirement in practice.

As discussed in Chapter 5, RWSTUKF outperforms RLS in terms of estimation accuracy. Therefore, it is proposed to combine RWSTUKF with the fault detection strategy to improve the performance of rupture detection. The proposed RWSTUKF-based fault detection method not only has the improved performance for rupture detection but also does not require prior knowledge of the statistics of puncture force.

6.3.3.1. *RWSTUKF based fault detection*

The rupture event is detected by the following hypothesis test:

- Null hypothesis $\mathcal{H}_0$: the system is in the normal condition.
- Alternative hypothesis $\mathcal{H}_1$: The system is experiencing a rupture event.

$$\begin{cases} \mathcal{H}_0 : \psi = \psi_0 \; at \; the \; normal \; condition \\ \mathcal{H}_1 : \psi = \psi_1 \; at \; runtpure \; event \end{cases} \tag{6-1}$$

The initial value of the parameter ψ is ψ_0 which indicates the normal condition. When a rupture event occurred, the value is changed to ψ_1. The hypothesis in (6-1) is tested with a distance measurement which is calculated with residual ε_k. In the proposed RWSTUKF-based fault detection, the residual ε_k is defined by the estimation error, which is the difference between the estimation of RWSTUKF and the actual measurement. Since the direct measurement of each parameter is not available, reconstructed force is calculated with the estimated parameters of the H-C model to calculate the residual. Thus, we have

$$\varepsilon_k = f_{\hat{x}_k} - f_{m_k} \tag{6-2}$$

where $f_{\hat{x}_k}$ is the reconstructed force based on the estimated parameters at time epoch t_k and $f_{m_k}$is measured force at epoch t_k.

Accordingly, the distance measurement can be defined as

$$Ee_k = {\varepsilon_k}^T P_{\bar{y}_k}^{-1} \varepsilon_k \tag{6-3}$$

where $P_{\bar{y}_k}^{-1}$ is the inverse of predicted measurement covariance.

For a given threshold T, if the distance measurement is larger than T, the hypothesis $\mathcal{H}_0$is held, leading to the detection of a rupture event, i.e.

$$\begin{cases} \psi_0 : Ee_k < T \ at \ the \ normal \ condition \\ \psi_1 : Ee_k \geq T \ at \ runtpure \ event \end{cases} \quad (6\text{-}4)$$

6.3.3.2. *Simulation analysis*

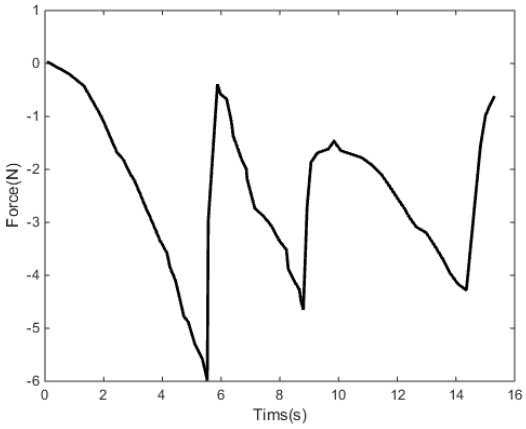

Figure 6-9 Evolution of the interaction forces from literature [27]

Simulations were conducted by using force data in the literature [27] to verify the proposed RWSTUKF-based fault detection method for rupture detection. The interaction force data was measured when a needle was inserted into the porcine liver through the skin [27]. There were three distinctive fast force transitions. The first and second fast force transitions (at $t_k = 5.53s$ and $t_k = 8.80s$) were rupture events. They were generated when the needle was penetrating the skin and liver, respectively. However, the last abrupt change in the force signal (at $t_k = 14.36s$) is not a rupture event. It was generated when the needle was being extracted at a fast speed.

Figure 6-10 represents the evolution of distance measurement which is calculated with force transition $(f_{k-1} - f_k)^2$ based on the direct filtering method. It is clear that the distance measurement at the first rupture point shows a significant difference. However, the distance measurement at the second rupture point is smaller than that at the last point due to the fast needle extraction. Apparently, if we use a threshold value to detect the second rupture, the peak point due to the fast needle extraction would also be identified as a rupture point.

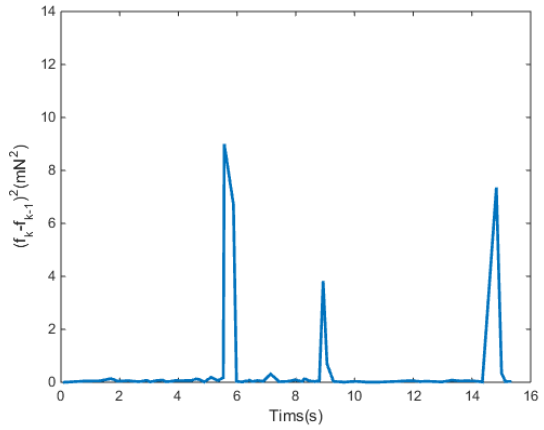

Figure 6-10 Distance measurement by the direct filtering

Trials were also conducted to evaluate the performance of the proposed RWSTUKF-based fault detection in the comparison with RLS-based fault detection [27]. As discussed in Chapter 3, the H-C model has to be linearized in order to be employed with the RLS. Figure 6-11 shows the distance measurement (Ep_k) by the RLS-based fault detection method. The distance measurement at the second rupture point is larger than that of the fast extraction. However, the differences between these two values are not significant (0.7mN), leading to the difficulty in rupture detection. In contrast, as shown in Figure 6-12, the distance

measurement by RWSTUKF-based fault detection has a clear difference (3mN) between these two values. This is because the estimated parameters by RWSTUKF are more precise and have less measurement noise. Therefore, we can easily distinguish the two rupture points from the non-rupture peak point due to the fast needle extraction with a threshold value.

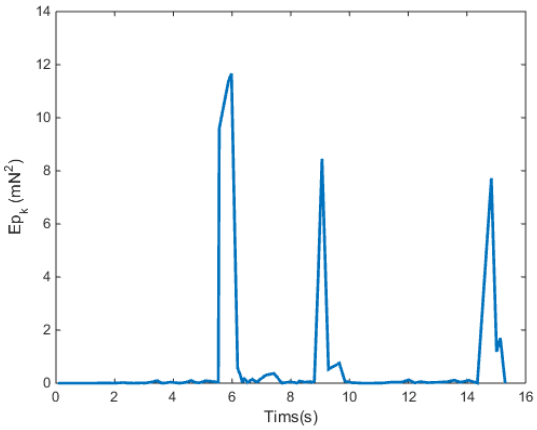

Figure 6-11 Distance measurement by RLS based fault detection

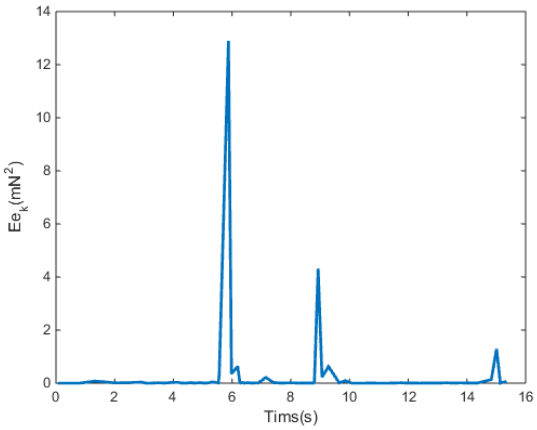

Figure 6-12 Distance measurement by RWSTUKF based fault detection

6.3.3.3. *Rupture detection in robotic needle insertion*

Trials were conducted using the master-slave robotic system to detect rupture events during robotic needle insertion. The experimental procedure was similar to that described in Section 6.3.2 except that the needle is extracted from the porcine liver sample at a fast speed to create a non-rupture peak point in the force signal.

The liver is covered by membrane, and has complex networks of veins inside [67]. The abrupt changes in interaction force signal occur when a needle penetrates membranes and veins. However, the fast force transition is also witnessed when the needle is extracted at a fast speed. Figure 6-13 represents the measured interaction force when a needle was inserted in the constant speed at 5 mm/s and extracted at the fast speed at 50 mm/s. Since the porcine liver is covered by a membrane, and has a complex network of veins inside [67], the needle penetrated the liver membrane at first and then pierced the vein network during the robotic needle insertion, leading to the two abrupt changes in the force profile as shown in Figure 6-13. When the needle penetrated the membrane of the porcine liver, a large abrupt change occurred at point **A** (t_k = 5.96s). When the needle penetrated the vein network, a small abrupt change was occurred at point **B** (t_k = 6.61s). Further, when the needle was extracted at a fast speed, an abrupt change, was also occurred at point **C** (t_k = 8.87s). However, point **C** does not correspond to a rupture event.

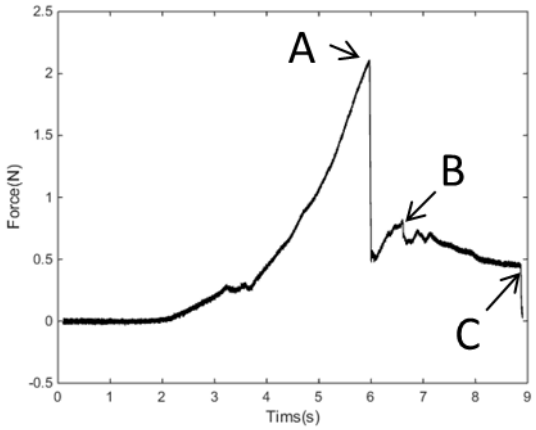

Figure 6-13 Force profile from a needle insertion with fast extraction

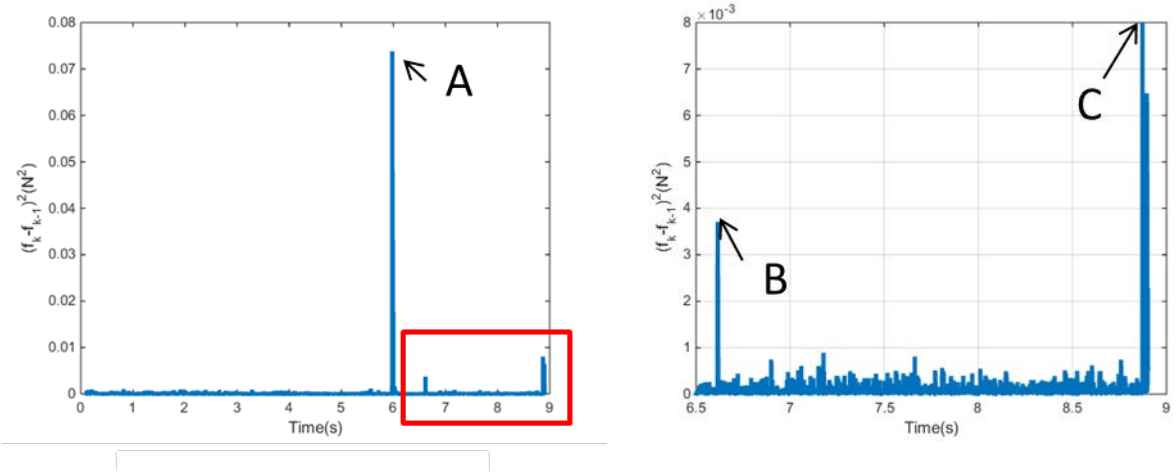

(a) (b)

Figure 6-14 (a) distance measurement by the direct filtering within the entire test period; (b) an enlarged view of the distance measurement within the time period from 6.5s to 9s

For comparison analysis, trials were conducted by the direct filtering, RLS-based fault detection and RWSTUK-based fault detection, respectively. As shown in Figure 6-14 (a), Figure 6-15 (a) and Figure 6-16 (a), point **A** is outstanding in the force profiles. Thus, all the three methods can clearly identify this rupture point **A**. However, as shown in Figure 6-14, since the distance measurement at point **C** is larger than that at point **B**, the direct filtering

method is unable to distinguish the second rupture point **B** and the non-rupture point **C** caused by the fast needle extraction.

Figure 6-15 represents the distance measurement by RLS-based fault detection. Although the distance measurement at the non-rupture rupture point **C** is smaller than that at the second point **B**, this difference is not significant, leading to the difficulty in distinguishing them.

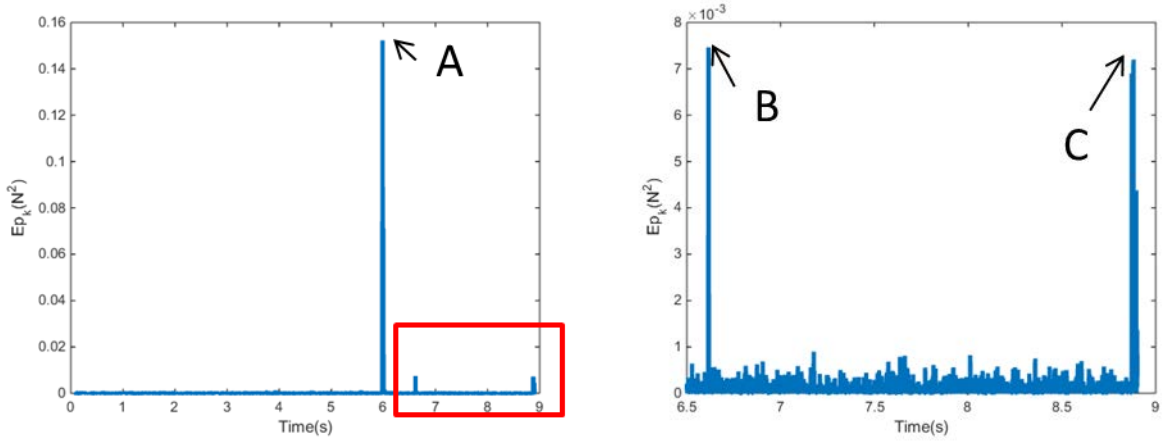

(a) (b)

Figure 6-15 (a) distance measurement by RLS based fault detection within the entire test period; (b) an enlarged view of the distance measurement within the time period from 6.5s to 9s

Figure 6-16 represents the distance measurement by RWSTUKF-based fault detection. It is clear that there is a distinctive difference between the two distance measurements at points **B** and **C.** Since the difference is clear, it is easy to distinguish the second rupture point **B** from the non-rupture point **C** by selecting a reasonable threshold. This is because RWSTUKF provides higher estimation accuracy than RLS, leading to the improved performance for rupture detection during needle insertion.

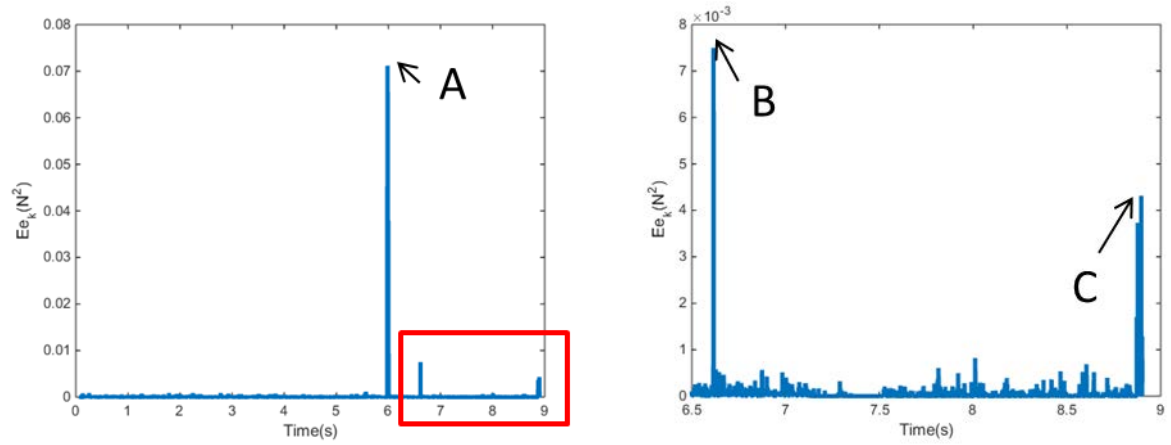

(a) (b)

Figure 6-16 (a) distance measurement by RWSTUKF based fault detection within the entire test period; (b) an enlarged view of the distance measurement within the time period from 6.5s to 9s

6.4. Summary

A bilateral master-slave robotic system has been developed for online soft tissue characterization by using UKF, RAUKF, and RWSTUKF as nonlinear state observers. Comparison analyses have been conducted through robotic indentation and needle insertion. It was demonstrated that RWSTUKF outperforms the other methods for the both cases. Further, a rupture detection approach was established based on RWSTUKF and integrated into the master-slave robotic system to detect rupture events that occurred in needle insertion. Simulations and experiments demonstrated that the proposed RWSTUKF-based fault detection has a better rupture detection performance than RLS based fault detection.

7. Conclusions and future work

7.1 Conclusions

This thesis is a study of online soft tissue characterization methods for RAMIS. The new method has been proposed with an integration of the UKF and the H-C model. It has been shown that the UKF is more suitable than the RLS as a parameter estimation method for RAMIS. For the next step, two uncertain conditions were considered: unknown noise statistics and model error. The adaptive UKF method was proposed to address the problem of unknown noise statistics. This method was further improved with a recursion method as RAUKF. To reduce the estimation inaccuracy caused by the model error, RWSTUKF was proposed. Finally, the needle insertion robot with the rupture detection was developed to verify that the proposed methods can be practical solutions in medical applications as a nonlinear state observer.

In Chapter 3, the H-C model with the UKF method has shown the better estimation performance than the conventional method (i.e. RLS) in terms of soft tissue characterization. In particular, one of the nonlinear parameters p in the H-C model was able to be considered as a variable with the UKF-based estimator whereas the RLS approach should consider the p as a unity (p=1). The simulation results showed that considering the parameter p as a variable with UKF leads to the better estimation. Although the estimation accuracy was improved by considering the p as a variable, the performance of the UKF system became more sensitive to the accuracy of system and measurement noise covariances. Both noise covariances were selected in an empirical way for the simulation in Chapter 3. However, the

empirical method would be difficult to be considered in some applications. This difficulty leads to extend the proposed method in Chapter 3 as an adaptive UKF method in Chapter 4.

In Chapter 4, the problem of the unknown noise statistics of the UKF-based estimator was tackled with an adaptive UKF concept (AUKF). The noise covariances were updated in real time in the AUKF instead of using constant noise covariances. A noise covariance estimator was developed based on the covariance matching technique with the windowing approximation method. However, the estimated noise covariance involves oscillations during an entire simulation because of the limited sample data within a small window. Therefore, RAUKF was proposed to reduce the oscillation in the estimated covariances. The RAUKF was able to improve the accuracy of noise covariance estimation by introducing the recursion concept. Simulations were conducted to verify that the accuracy of noise covariance estimation is significantly improved with RAUKF. In addition, the state estimation performance is also improved based on the correct noise covariance estimation.

In Chapter 5, the problem of the model error of the UKF-based estimator was addressed. The proposed UKF with the H-C model method for an online soft tissue characterization method was further improved to keep the high accurate estimation performance in the presence of a model error. RWSTUKF was proposed to adjust the predicted state covariance with the random weighting concept to compensate model error. The predicted state covariance represents the confidence of how much we can trust our system model. The value of predicted state covariance has to be modified in the presence of a model error. However, it would be difficult to determine the best value of the predicted state covariance to precisely compensate the effect of model error. The proposed RWSTUKF uses an

orthogonality principle to find the best value of the predicted state covariance with the assumption the estimation error only caused by model errors. Based on simulation results, it can be seen that the proposed method can obtain satisfactory estimation results even in the presence of a model error.

Finally, a master-slave robotic system has been developed for a medical application by using the proposed online soft tissue characterization methods as a nonlinear state observer. Both experiments of robotic indentation and needle insertion were conducted, demonstrating that the RWSTUKF has the best estimation performance than the others (RLS, UKF and RAUKF). Based on the experiment results, an RWSTUKF-based fault detection method was further established for rupture detection during robotic needle insertion. Simulation and experimental results demonstrated that the proposed RWSTUKF-based fault detection has a better performance than RLS-based fault detection for rupture detection in robotic needle insertion.

7.2 Future work

The proposed methods (UKF, RAUKF and RWSTUKF), based on the H-C model for soft tissue characterization, require the selection of sigma points for parameter estimation. This thesis employs a simple method to select the sigma points with (3-13) [35]. However, different methods have been proposed for selecting the sigma points, such as the simplex unscented transformation [68] for computational efficiency or the spherical unscented transformation [69] for numerical stability. In the future, the investigation of the issue of sigma-point

selection will be conducted to establish a new sigma-point selection algorithm to further improve the performance of the proposed soft tissue characterization methods.

RAUKF proposed in Chapter 4 updates system or measurement noise covariance at every time point according to state estimation error. Although RAUKF has the improved performance comparing to the conventional UKF, the RAUKF is established based on the assumption that state estimation errors are only caused by inaccurate noise covariance. However, state estimation error can be caused by other factors, such as model uncertainty described in Chapter 5. Therefore, it is necessary to distinguish the source of estimation error, such as inaccurate noise covariance, physiological conditions, different surgical conditions, and external interference. In the future, a multiple-model Kalman filter (Multiple-model Kalman filter [70] is a method to characterize the probability of system behaviour using likelihood function) will be considered to differentiate the error of inaccurate noise covariance from other error sources and further combined this filter with RAUKF for online soft tissue characterization.

RWSTUKF proposed in Chapter 5 only considers model error existed in the system model. However, the model error also exists in the measurement model as well. The proposed RWSTUKF method for the system model will be extended to the measurement model, and thus new theories and algorithms of RWSTUKF estimation will be established for soft tissue characterization.

RWSTUKF accounts for the system model error with the scaling factor which is determined by balancing predicted state covariance with its theoretical value. In theory, this guarantees the achieved estimation is optimal with minimum error, i.e., the error magnitude is

bounded by a certain threshold value. This threshold value can be identified using a large volume of empirical test data or by a statistical approach such linear regression or machine learning algorithm.

The proposed methods in Chapter 4 (RAUKF) and Chapter 5 (RWSTUKF) improve the performance of the UKF. RAUKF was concerned about the effect of inaccurate noise statistics only, whereas RWSTUKF the effect of inaccurate system model only. However, both problems could exist in a system thus they are required to be distinguished. In the future, an error classifier will be developed to distinguish the error type. Further, a hybrid method will be established to selectively apply RAUKF and RWSTUKF according to the error type identified by the estimation error classifier for soft tissue characterization. Although it would be difficult to develop an error classifier to separate the source of estimation error as individual parts since the calculated estimation error is the sum of estimation errors by those two inaccuracies, it would be possible to develop an error classifier to determine the main source of the estimation error through a large volume of test data sets. We could minimize the effect of inaccuracies efficiently to apply RAUKF or RWSTUKF depending on the type of error source with the error classifier.

The current developed master-slave robotic system is one DOF system. In the future, this system will also be extended to six DOFs for a wide range of medical applications.

References

[1] I. Surgical, "The da Vinci surgical system," *Intuitive Surgical Inc., Sunnyvale, CA, available at: http://www. intuitivesurgical. com,* 2013.

[2] I. Elgezua, Y. Kobayashi, and M. G. Fujie, "Survey on current state-of-the-art in needle insertion robots: open challenges for application in real surgery," *Procedia CIrP,* vol. 5, pp. 94-99, 2013.

[3] B. Rocco, D. V. Matei, S. Melegari, J. C. Ospina, F. Mazzoleni, G. Errico*, et al.*, "Robotic vs open prostatectomy in a laparoscopically naive centre: A matched-pair analysis," *BJU international,* vol. 104, pp. 991-995, 2009.

[4] J. Miller, A. Smith, E. Kouba, E. Wallen, and R. S. Pruthi, "Prospective evaluation of short-term impact and recovery of health related quality of life in men undergoing robotic assisted laparoscopic radical prostatectomy versus open radical prostatectomy," *The Journal of urology,* vol. 178, pp. 854-859, 2007.

[5] B. M. Smithers, D. C. Gotley, I. Martin, and J. M. Thomas, "Comparison of the outcomes between open and minimally invasive esophagectomy," *Annals of surgery,* vol. 245, pp. 232-240, 2007.

[6] N. Enayati, E. De Momi, and G. Ferrigno, "Haptics in robot-assisted surgery: challenges and benefits," *IEEE reviews in biomedical engineering,* vol. 9, pp. 49-65, 2016.

[7] A. M. Okamura, "Haptic feedback in robot-assisted minimally invasive surgery," *Current opinion in urology,* vol. 19, p. 102, 2009.

[8] C. D. Wickens, "Multiple resources and performance prediction," *Theoretical Issues in Ergonomics Science,* vol. 3, pp. 159-177, 2002/01/01 2002.

[9] K. Bark, W. McMahan, A. Remington, J. Gewirtz, A. Wedmid, D. I. Lee*, et al.*, "In vivo validation of a system for haptic feedback of tool vibrations in robotic surgery," *Surgical Endoscopy,* vol. 27, pp. 656-664, 2013.

[10] I. Nisky, A. Pressman, C. M. Pugh, F. A. Mussa-Ivaldi, and A. Karniel, "Perception and action in teleoperated needle insertion," *IEEE transactions on haptics,* vol. 4, pp. 155-166, 2011.

[11] H. I. Son, T. Bhattacharjee, and H. Hashimoto, "Enhancement in operator's perception of soft tissue and its experimental validation for scaled teleoperation systems," *IEEE/ASME Transactions on Mechatronics,* vol. 16, pp. 1096-1109, 2011.

[12] M. Soroush, "Nonlinear state-observer design with application to reactors," *Chemical Engineering Science,* vol. 52, pp. 387-404, 1997.

[13] C. Mitsantisuk, K. Ohishi, and S. Katsura, "Estimation of Action/Reaction Forces for the Bilateral Control Using Kalman Filter," *IEEE Transactions on Industrial Electronics,* vol. 59, pp. 4383--4393, 2012.

[14] G. Luders and K. Narendra, "An adaptive observer and identifier for a linear system," *IEEE Transactions on Automatic Control,* vol. 18, pp. 496-499, 1973.

[15] Y. Ohba, M. Sazawa, K. Ohishi, T. Asai, K. Majima, Y. Yoshizawa*, et al.*, "Sensorless force control for injection molding machine using reaction torque observer considering torsion phenomenon," *IEEE Transactions on Industrial Electronics,* vol. 56, pp. 2955-2960, 2009.

[16] A. Haddadi and K. Hashtrudi-Zaad, "Real-time identification of Hunt–Crossley dynamic models of contact environments," *IEEE Transactions on Robotics,* vol. 28, pp. 555-566, 2012.

[17] I. Peterlík, M. Sedef, C. Basdogan, and L. Matyska, "Real-time visio-haptic interaction with static soft tissue models having geometric and material nonlinearity," *Computers & Graphics,* vol. 34, pp. 43-54, 2010.

[18] G. Bastin and M. Gevers, "Stable adaptive observers for nonlinear time-varying systems," *IEEE Transactions on Automatic Control,* vol. 33, pp. 650-658, 1988.

[19] R. Marino and P. Tomei, "Global adaptive observers for nonlinear systems via filtered transformations," *IEEE Transactions on Automatic Control,* vol. 37, pp. 1239-1245, 1992.
[20] D. Wang, F. Ding, and L. Ximei, "Least squares algorithm for an input nonlinear system with a dynamic subspace state space model," *Nonlinear Dynamics,* vol. 75, pp. 49-61, 2014.
[21] X. Wang and F. Ding, "Recursive parameter and state estimation for an input nonlinear state space system using the hierarchical identification principle," *Signal Processing,* vol. 117, pp. 208-218, 2015.
[22] S. J. Julier and J. K. Uhlmann, "Unscented filtering and nonlinear estimation," *Proceedings of the IEEE,* vol. 92, pp. 401-422, 2004.
[23] H. E. Soken and C. Hajiyev, "Adaptive fading UKF with Q-adaptation: application to picosatellite attitude estimation," *Journal of Aerospace Engineering,* vol. 26, pp. 628-636, 2011.
[24] W.-B. Yang and S.-Y. Li, "Autonomous navigation filtering algorithm for spacecraft based on strong tracking UKF," *Systems Engineering and Electronics,* vol. 33, pp. 2485-2491, 2011.
[25] D.-J. Jwo and S.-Y. Lai, "Navigation integration using the fuzzy strong tracking unscented Kalman filter," *Journal of Navigation,* vol. 62, pp. 303-322, 2009.
[26] Y.-P. Zheng and A. F. Mak, "An ultrasound indentation system for biomechanical properties assessment of soft tissue in-vivo," *IEEE Transactions on Biomedical Engineering,* vol. 43, pp. 912-918, 1996.
[27] L. Barbé, B. Bayle, M. de Mathelin, and A. Gangi, "In vivo model estimation and haptic characterization of needle insertions," *The International Journal of Robotics Research,* vol. 26, pp. 1283-1301, 2007.
[28] A. Haddadi and K. Hashtrudi-Zaad, "A new method for online parameter estimation of hunt-crossley environment dynamic models," in *2008 IEEE/RSJ International Conference on Intelligent Robots and Systems*, 2008, pp. 981-986.
[29] N. Diolaiti, C. Melchiorri, and S. Stramigioli, "Contact impedance estimation for robotic systems," *IEEE Transactions on Robotics,* vol. 21, pp. 925-935, 2005.
[30] H. B. Liu, K. Sangpradit, M. Li, P. Dasgupta, K. Althoefer, and L. D. Seneviratne, "Inverse finite-element modeling for tissue parameter identification using a rolling indentation probe," *Medical & Biological Engineering & Computing,* vol. 52, pp. 17-28, Jan 2014.
[31] T. Hoshi, Y. Kobayashi, K. Kawamura, and M. G. Fujie, "Developing an intraoperative methodology using the finite element method and the extended kalman filter to identify the material parameters of an organ model," in *2007 29th Annual International Conference of the IEEE Engineering in Medicine and Biology Society*, 2007, pp. 469-474.
[32] M. S. Grewal, A. P. Andrews, and A. K. Filtering, "Theory and practice using MATLAB," *Wieley-Interscience, Canada,* 2001.
[33] A. H. Jazwinski, *Stochastic processes and filtering theory*: Courier Corporation, 2007.
[34] S. Gao, G. Hu, and Y. Zhong, "Windowing and random weighting-based adaptive unscented Kalman filter," *International Journal of Adaptive Control and Signal Processing,* vol. 29, pp. 201-223, 2015.
[35] S. J. Julier and J. K. Uhlmann, "New extension of the Kalman filter to nonlinear systems," in *AeroSense'97*, 1997, pp. 182-193.
[36] J. M. Pak, C. K. Ahn, P. Shi, and M. T. Lim, "Self-recovering extended Kalman filtering algorithm based on model-based diagnosis and resetting using an assisting FIR filter," *Neurocomputing,* vol. 173, pp. 645-658, 2016.
[37] F. Sun, X. Hu, Y. Zou, and S. Li, "Adaptive unscented Kalman filtering for state of charge estimation of a lithium-ion battery for electric vehicles," *Energy,* vol. 36, pp. 3531-3540, 2011.
[38] Y. Yang and T. Xu, "An adaptive Kalman filter based on Sage windowing weights and variance components," *The Journal of Navigation,* vol. 56, pp. 231-240, 2003.

[39] W. Gao, H. He, and J. Chen, "An adaptive UKF algorithm and its application for GPS-INS integrated navigation system," *Trans. Beijing Ins. Technol,* vol. 28, pp. 505-509, 2008.

[40] Y. Shi, C. Han, and Y. Liang, "Adaptive UKF for target tracking with unknown process noise statistics," in *Information Fusion, 2009. FUSION'09. 12th International Conference on*, 2009, pp. 1815-1820.

[41] X. Wang, X. Zhao, and X. Yang, "Research of Motion Resolving and Filtering Algorithm of a Ship's Three-Freedom Motion Simulation Platform Based on LabVIEW," in *Journal of Physics: Conference Series*, 2006, p. 149.

[42] T. Yamamoto, N. Abolhassani, S. Jung, A. M. Okamura, and T. N. Judkins, "Augmented reality and haptic interfaces for robot-assisted surgery," *The International Journal of Medical Robotics and Computer Assisted Surgery,* vol. 8, pp. 45-56, 2012.

[43] B. Yalcin and K. Ohnishi, "Infinite-Mode Networks for Motion Control," *IEEE Transactions on Industrial Electronics,* vol. 56, pp. 2933-2944, 2009.

[44] M. Hashizume, M. Shimada, M. Tomikawa, Y. Ikeda, I. Takahashi, R. Abe*, et al.*, "Early experiences of endoscopic procedures in general surgery assisted by a computer-enhanced surgical system," *Surgical Endoscopy and Other Interventional Techniques,* vol. 16, pp. 1187-1191, 2002.

[45] Y. Kasahara, H. Kawana, S. Usuda, and K. Ohnishi, "Telerobotic-assisted bone-drilling system using bilateral control with feed operation scaling and cutting force scaling," *The International Journal of Medical Robotics and Computer Assisted Surgery,* vol. 8, pp. 221-229, 2012.

[46] H. Tanaka, K. Ohnishi, H. Nishi, T. Kawai, Y. Morikawa, S. Ozawa*, et al.*, "Implementation of bilateral control system based on acceleration control using FPGA for multi-DOF haptic endoscopic surgery robot," *IEEE Transactions on Industrial Electronics,* vol. 56, pp. 618-627, 2009.

[47] D. A. Lawrence, "Stability and transparency in bilateral teleoperation," *IEEE Transactions on Robotics and Automation,* vol. 9, pp. 624-637, 1993.

[48] L. Chan, F. Naghdy, D. Stirling, and M. Field, "Nonlinear bilateral teleoperation using extended active observer for force estimation and disturbance suppression," *Robotica,* vol. 33, pp. 61-86, 2015.

[49] H. I. Son, T. Bhattacharjee, and D. Y. Lee, "Estimation of environmental force for the haptic interface of robotic surgery," *Journal of Medical Robotics,* vol. 6, pp. 221--230, 2010.

[50] J. Jung, J. Lee, and K. Huh, "Robust contact force estimation for robot manipulators in three-dimensional space," *Proceedings of the Institution of Mechanical Engineers, Part C: Journal of Mechanical Engineering Science,* vol. 220, pp. 1317-1327, 2006.

[51] K. Hashtrudi-Zaad and S. E. Salcudean, "Analysis of control architectures for teleoperation systems with impedance/admittance master and slave manipulators," *The International Journal of Robotics Research,* vol. 20, pp. 419-445, 2001.

[52] K. Hunt and F. Crossley, "Coefficient of restitution interpreted as damping in vibroimpact," *Journal of Applied Mechanics,* vol. 42, pp. 440-445, 1975.

[53] R. E. Kalman, "A new approach to linear filtering and prediction problems," *Journal of basic Engineering,* vol. 82, pp. 35-45, 1960.

[54] A. Asadian, M. R. Kermani, and R. V. Patel, "A novel force modeling scheme for needle insertion using multiple Kalman filters," *IEEE Transactions on Instrumentation and Measurement,* vol. 61, pp. 429-438, 2012.

[55] A. M. Okamura, C. Simone, and M. D. O'Leary, "Force modeling for needle insertion into soft tissue," *IEEE Transactions on Biomedical Engineering,* vol. 51, pp. 1707-1716, 2004.

[56] A. Mohamed and K. Schwarz, "Adaptive Kalman filtering for INS/GPS," *Journal of Geodesy,* vol. 73, pp. 193-203, 1999.

[57] K. Myers and B. Tapley, "Adaptive sequential estimation with unknown noise statistics," *IEEE Transactions on Automatic Control,* vol. 21, pp. 520-523, 1976.
[58] Z. Deng and Y. Guo, "Dynamic Prediction of Oil Output and Water Output in Oil Field," *Acta Automatica Sinica,* vol. 9, pp. 121-126, 1983.
[59] M. Mahvash and V. Hayward, "Haptic rendering of cutting: A fracture mechanics approach," 2001.
[60] M. Mahvash and P. E. Dupont, "Mechanics of dynamic needle insertion into a biological material," *IEEE Transactions on Biomedical Engineering,* vol. 57, pp. 934-943, 2010.
[61] J. L. Sparks, N. A. Vavalle, K. E. Kasting, B. Long, M. L. Tanaka, P. A. Sanger*, et al.*, "Use of Silicone Materials to Simulate Tissue Biomechanics as Related to Deep Tissue Injury," *Advances in Skin & Wound Care,* vol. 28, pp. 59-68, 2015.
[62] S. Gao, Z. Feng, Y. Zhong, and B. Shirinzadeh, "Random weighting estimation of parameters in generalized Gaussian distribution," *Information Sciences,* vol. 178, pp. 2275-2281, 2008.
[63] S. Gao, Z. Zhang, and B. Yang, "The random weighting estimate of quantile process," *Information Sciences,* vol. 164, pp. 139-146, 2004.
[64] T. Kailath, "An innovations approach to least-squares estimation--Part I: Linear filtering in additive white noise," *IEEE transactions on automatic control,* vol. 13, pp. 646-655, 1968.
[65] O. PHANTOM, "SensAble Technologies," *Inc., http://www. sensable. com*.
[66] B. Bayle, M. Joinie-Maurin, L. Barbe, J. Gangloff, and M. De Mathelin, "Robot interaction control in medicine and surgery: Original results and open problems," in *Computational Surgery and Dual Training*, ed: Springer, 2014, pp. 169-191.
[67] I. Elgezua, S. Song, Y. Kobayashi, and M. G. Fujie, "Online Event Classification for Liver Needle Insertion Based on Force Patterns," in *Intelligent Autonomous Systems 13*, ed: Springer, 2016, pp. 1145-1157.
[68] S. J. Julier and J. K. Uhlmann, "Reduced sigma point filters for the propagation of means and covariances through nonlinear transformations," in *American Control Conference, 2002. Proceedings of the 2002*, 2002, pp. 887-892.
[69] S. J. Julier, "The spherical simplex unscented transformation," in *American Control Conference, 2003. Proceedings of the 2003*, 2003, pp. 2430-2434.
[70] K. Xiong, T. Liang, and L. Yongjun, "Multiple model Kalman filter for attitude determination of precision pointing spacecraft," *Acta Astronautica,* vol. 68, pp. 843-852, 2011.